JBC Papers in Press. Published on February 26, 2018 as Manuscript M117.817700
The latest version is at http://www.jbc.org/cgi/doi/10.1074/jbc.M117.817700

Comparative and integrative metabolomics reveal that *S*-nitrosation inhibits physiologically relevant metabolic enzymes

Joel J. Bruegger,[a] Brian C. Smith,[a] Sarah L. Wynia-Smith,[a] Michael A. Marletta*[a,b]

From the [a]QB3 Institute, University of California, Berkeley, 356 Stanley Hall, Berkeley, California, 94720-3220, United States and the [b]Department of Chemistry, and the Department of Molecular and Cell Biology, University of California, Berkeley, 374B Stanley Hall, Berkeley, California 94720-3220, United States

Running Title: *S-nitrosation modifies metabolic enzyme function*

To whom correspondence should be addressed: Michael A. Marletta, QB3 Institute, University of California, Berkeley, 374B Stanley Hall, Berkeley, California 94720-3220. Telephone: (510) 642-8758 E-mail: marletta@berkeley.edu

Keywords: *S*-nitrosylation, metabolomics, proteomics, nitric oxide, metabolism, enzyme kinetics.

ABSTRACT

Cysteine *S*-nitrosation is a reversible posttranslational modification mediated by nitric oxide (•NO)-derived agents. *S*-nitrosation participates in cellular signaling and is associated with several diseases such as cancer, cardiovascular diseases, and neuronal disorders. Despite the physiological importance of this nonclassical •NO signaling pathway, little is understood about how much *S*-nitrosation affects protein function. Moreover, identifying physiologically relevant targets of *S*-nitrosation is difficult because of the dynamics of transnitrosation and a limited understanding of the physiological mechanisms leading to selective protein *S*-nitrosation. To identify proteins whose activities are modulated by *S*-nitrosation, we performed a metabolomics study comparing wild-type and endothelial nitric oxide synthase (eNOS) knockout mice. We integrated our results with those of a previous proteomics study that identified physiologically relevant *S*-nitrosated cysteines, and we found that the activity of at least 21 metabolic enzymes might be regulated by *S*-nitrosation. We cloned, expressed, and purified four of these enzymes and observed that *S*-nitrosation inhibits the metabolic enzymes 6-phosphogluconate dehydrogenase (6PGD), Δ1-pyrroline-5-carboxylate dehydrogenase (ALDH4A1), catechol-*O*-methyltransferase (COMT), and D-3-phosphoglycerate dehydrogenase (PHGDH). Furthermore, using site-directed mutagenesis, we identified the predominate cysteine residue influencing the observed activity changes in each enzyme. In summary, using an integrated metabolomics approach, we have identified several physiologically relevant *S*-nitrosation targets, including metabolic enzymes, which are inhibited by this modification, and have found the cysteines modified by *S*-nitrosation in each enzyme.

Nitric oxide (•NO) is an important signaling molecule in vertebrate tissue that controls physiological processes including vasodilation, neurotransmission, and platelet aggregation (1-3). •NO is biosynthesized by the three mammalian isoforms of nitric oxide synthase (NOS). Endothelial (eNOS) and neuronal NOS (nNOS) produce picomolar to nanomolar concentrations of •NO for cellular signaling, while inducible NOS (iNOS) produces •NO at cytotoxic concentrations in the low micromolar range at sites of infection (4, 5). The most thoroughly characterized •NO signaling pathway involves the enzyme soluble guanylate cyclase (sGC) (6). •NO produced by NOS freely diffuses into adjacent cells where it activates sGC to increase the concentration of the secondary messenger cyclic guanosine monophosphate (cGMP) that activates downstream signaling pathways.

Another important, though less well understood, signaling mechanism involving •NO is cysteine *S*-nitrosation. *S*-nitrosation is a post-translational modification of cysteine residues by which an *S*-nitrosothiol is initially formed via a one-electron oxidation. Once formed, *S*-nitrosothiols can be transferred through an intermediate transnitrosating agent such as *S*-nitrosoglutathione (GSNO) (7). Many studies have corroborated the influence of *S*-nitrosation on protein and tissue function, as well as the variation of *S*-nitrosation profiles in disease states. However, the roles of *S*-nitrosation in cellular signaling pathways remain poorly understood (8-11). If *S*-nitrosation participates in cellular signaling and is not simply a result of nitrosative stress, the cellular levels of protein *S*-nitrosation must be tightly controlled (12). In this sense, *S*-nitrosation is often compared to *O*-phosphorylation, where a kinase transfers a phosphoryl moiety to an acceptor amino acid from an ATP donor molecule, which then changes the function or activity of the enzyme target (13). Phosphatases then act to reverse the process by hydrolytically removing the phosphoryl group. Similarly, in *S*-nitrosation, a NO-derived agent transfers •NO (formally NO^+) to a cysteine residue, potentially altering protein function. Unlike phosphorylation, however, many key details remain unknown.

While there is a growing body of evidence that *S*-nitrosation has a role in signaling mechanisms, relatively few validated protein targets of *S*-nitrosation have been characterized (14-17). Targets of *S*-nitrosation identified while using exogenous NO-donors are difficult to establish as physiologically relevant due to the high reactivity and low specificity of NO-derived agents. This is also complicated because the *in vivo* mechanisms of *S*-nitrosation and primary NO-donor sources are unknown (18-22). To eliminate the problems associated with the use of an exogenous •NO donor, Ischiropoulos and coworkers (23) identified sites of protein *S*-nitrosation through a proteomic comparison of wild-type and eNOS knockout ($eNOS^{-/-}$) mice. In this study, unmodified cysteine residues were first blocked with methyl methanethiosulfonate (MMTS), then *S*-nitrosated proteins were enriched with an organomercury resin. Bound proteins were subjected to on-resin trypsin digestion and bound peptides containing the *S*-nitrosated cysteine residue were eluted by oxidation with performic acid to generate sulfonic acids at the *S*-nitrosated cysteine residue followed by LC-MS/MS analysis to identify *S*-nitrosated protein cysteine residues. Efficient cysteine blocking with MMTS is essential to the success of this approach as any unblocked cysteine residue will also be bound by the mercury resin and increase the background of the assay.

However, the functional relevance of the vast majority of these observed eNOS-dependent *S*-nitrosation targets is unknown. Some of the *S*-nitrosated cysteine residues could be highly reactive toward NO-derived agents simply due to increased cysteine sulfur nucleophilicity; however, *S*-nitrosation may also be involved in functional roles. For example, an *S*-nitrosated protein may serve as a transnitrosating agent, conferring specificity to a target cysteine of another protein. One example of this functionality is the transnitrosation of caspase-3 by thioredoxin (14). *S*-nitrosation could also play a role in protein localization and cellular transport (24). Due to changes in surface electrostatics, *S*-nitrosation can potentially disrupt or promote the formation of oligomers or other protein complexes. Lastly, *S*-nitrosation can directly inhibit or stimulate enzymatic activity.

In this study, complementary metabolomics of wild-type and $eNOS^{-/-}$ mice is reported. Analysis of the metabolic differences in conjunction with the previously published proteomics study led to the identification of 21 metabolic enzymes that may be modulated by *S*-nitrosation (23). These metabolic enzymes were found to be *S*-nitrosated in the previous proteomics study with upregulated substrate and downregulated product (or vice versa) in the metabolomics study reported here. Four of the 21 enzyme targets (6-phosphogluconate dehydrogenase, 6PGD; Δ^1-pyrroline-5-carboxylate dehydrogenase, ALDH4A1; catechol *O*-methyltransferase, COMT; and D-3-phosphoglycerate dehydrogenase, PHGDH) were studied *in vitro* for inhibitory effects by *S*-nitrosation. *S*-nitrosoglutathione (GSNO) was selected as the nitrosothiol donor because of its putative physiological role in transnitrosation

signaling (18, 25, 26), but it is important to note that GSNO may not be the relevant nitrosating agent that led to the observed *S*-nitrosation of these enzymes in mice. All four of the tested enzymes were inhibited upon GSNO treatment. Through site-directed mutagenesis, the cysteine residues responsible for modulating the activity were identified. Finally, after measuring the fraction of individual cysteine *S*-nitrosation, the degree of enzyme inhibition was confirmed to correlate with the amount of cysteine *S*-nitrosation. In summary, this study integrates comparative proteomics published previously with metabolomics performed in the current study and presents quantitative and functional analysis of metabolic enzymes with the primary goal of identifying physiologically relevant protein targets of *S*-nitrosation.

Results

Metabolomics complements previously published proteomics to identify functional sites of metabolic enzyme S-nitrosation–A recent proteomics study by Ischiropoulos and coworkers of wild-type and eNOS knockout mice identified 942 *S*-nitrosated cysteine residues that are eNOS-dependent (23). Over half of the cysteine residues identified were in metabolic enzymes (313 enzymes, some containing multiple *S*-nitrosated cysteine residues); however, the functional consequences of most of these *S*-nitrosation sites are unknown. To narrow the list of target enzymes to those whose activities are inhibited or activated by *S*-nitrosation, a metabolomics comparison of wild-type and eNOS knockout mice was carried out and putative metabolite changes were cross-referenced with the eNOS-dependent metabolic enzyme *S*-nitrosation sites identified by the Ischiropoulos proteomics study (23).

The approach to identify metabolic enzyme targets of *S*-nitrosation that are functionally-relevant is outlined in Figure 1. To parallel the proteomics study, we analyzed the brain, heart, kidney, liver, lung and pancreas (instead of the thymus). The combined data narrows down the metabolic enzyme targets of *S*-nitrosation to only those *S*-nitrosation sites that impact enzymatic activity. After obtaining a list of 176,035 mass features (observed monoisotopic m/z values with consistent retention times across all samples) of eluents from a C18 HPLC column analyzed separately by positive and negative mode mass spectrometry as well as a hydrophilic interaction chromatography (HILIC) column analyzed by negative mode mass spectrometry, the chromatograms of six biological replicates of each WT and *eNOS*$^{-/-}$ organ were analyzed and mass feature variations were compared using XCMS online (27-29). It is important to note that many of the observed mass features could match multiple metabolites, isotopes, or salt forms. As a result, mass features that shared no more than six potential metabolites were examined, as matched to metabolites in the METLIN database (30). These putative metabolites were then mapped to 71 KEGG metabolic pathway maps utilizing Pathos online (31, 32). *S*-nitrosated enzymes from the Ischiropoulos proteomic study (23) were then annotated with the metabolomics data. Forty-four *S*-nitrosated metabolic enzymes with more than 1.4-fold modulated product and substrate levels were identified (Table 1). Mass features with $p < 0.1$ (n = 6) when comparing differences in wild-type versus *eNOS*$^{-/-}$ mouse organ (note that each organ and type of LC-MS run were statistically compared separately) were then identified to narrow the list to 21 metabolic enzymes (Table S1; Figures 2B, 3B, 4B, and 5B).

Metabolic enzyme target list–To investigate the effect of *S*-nitrosation on metabolic activity, a subset of the identified enzyme targets was selected for further characterization. These enzymes were selected based on the following criteria: (*i*) confidence in metabolite identification as outlined above; (*ii*) conservation of *S*-nitrosated cysteine residue in vertebrates or species known to contain an eNOS isoform (Figure S1); (*iii*) established protocols for enzyme expression, purification, and activity determination; (*iv*) availability of enzyme crystal structure to map the site of *S*-nitrosation relative to the enzyme active site (Figures 2A, 3A, 4A, and 5A); *(v)* disease relevance of the metabolic enzyme; and *(vi)* evidence in the literature implying •NO involvement in the metabolic pathway. To relate findings to human health, human instead of mouse protein sequences were used for this study. Based on these criteria, the following four enzymes

were selected for *in vitro* determination of the effects of *S*-nitrosation: 6PGD, ALDH4A1, COMT, and PHGDH. Detailed descriptions of each enzyme can be found in the Supporting Information. Two control enzymes, aldolase A (ALDOA) and triose phosphate isomerase 1 (TPI1) (Figure 6), were selected for *in vitro* characterization. These control enzymes were *S*-nitrosated in the Ischiropoulos study (23), but did not fit our metabolomics criteria. For these two glycolytic enzymes, we anticipated that *S*-nitrosation would not modulate activity but could have another function in signaling (33, 34).

S-nitrosation-dependent inhibition of target enzymes–The activity of each enzyme was assayed as described in the Experimental Procedures section. Since specific physiological mechanisms of *S*-nitrosation for these target metabolic enzymes are unknown, the small-molecule transnitrosation donor GSNO was used. In *in vitro* studies, any accessible cysteine may be *S*-nitrosated, which may differ from specific *in vivo* targeted *S*-nitrosation reactions (35, 36). All enzymes were purified following recombinant overexpression in *E. coli* for *in vitro* characterization. To confirm each enzyme was *S*-nitrosated upon GSNO treatment, a TAMRA-maleimide switch assay was used, which is a variant of the biotin switch assay, where tetramethylrhodamine fluorescent imaging was substituted for a biotin immunoblot (37, 38). The enzymes 6PGD and PHGDH (at 20 and 150 μM, respectively), were incubated with 2 mM GSH or GSNO for 1 h at 37 ˚C; 20 μM ALDH4A1, ALDOA, and TPI1 were incubated with 1 mM GSH or GSNO for 1 h at 37˚C; and 20 μM COMT was incubated for 150 μM GSH or GSNO for 1 h at 37 ˚C. All enzymes were *S*-nitrosated after incubation with GSNO followed by buffer exchange to remove residual GSNO (Figures 2C, 3C, 4C, 5C, and 6A). To determine the effects of *S*-nitrosation on each enzyme, activity assays were performed after exposure to GSNO (or reduced glutathione, GSH, followed by buffer exchange to remove residual GSH) and data was analyzed under steady-state kinetic conditions (Table 2, Figure S2).

The specificity constant (k_{cat}/K_M) of 6PGD negative control (2 mM GSH-treated) was 0.68 $\mu M^{-1}s^{-1}$ while 6PGD activity when incubated with 2 mM GSNO was two orders of magnitude lower at 0.0057 $\mu M^{-1}s^{-1}$ (Figure 2D, Table 2). The k_{cat}/K_M value of ALDH4A1 treated with 1 mM GSH was 0.29 $\mu M^{-1}s^{-1}$ while *S*-nitrosation from 1 mM GSNO treatment lowered activity to 7% that of GSH-treated ALDH4A1 at 0.021 $\mu M^{-1}s^{-1}$ (Figure 3D, Table 2). Treatment of COMT with 150 μM GSNO resulted in 26% of the 150 μM GSH-treated activity with k_{cat}/K_M values decreasing from 0.55 to 0.14 $\mu M^{-1}min^{-1}$ (Figure 4D, Table 2). It should be noted that higher concentrations of GSNO incubated with COMT resulted in complete inhibition of enzyme activity. Finally, *S*-nitrosation of PHGDH resulted in 29% of the GSH-treated activity, decreasing from 0.070 $mM^{-1}s^{-1}$ to 0.021 $mM^{-1}s^{-1}$ with 2 mM GSNO (Figure 5D, Table 2). The control enzymes ALDOA and TPI1 were unaffected, giving the same k_{cat}/K_M values for both GSNO and GSH treatments within experimental error: 0.41 $\mu M^{-1}s^{-1}$ for ALDOA and 2.0 $\mu M^{-1}s^{-1}$ for TPI1 (Figure 6B, Table 2). In summary, the metabolic enzyme targets identified through the metabolomics study (6PGD, ALDH4A1, COMT, and PHGDH) were all inhibited when incubated with GSNO, while neither control enzyme (ALDOA and TPI1) showed significant inhibition with similar concentrations of GSNO as the target enzymes.

Identification of cysteine residues responsible for metabolic enzyme inhibition–The four enzyme targets (6PGD, ALDH4A1, COMT, and PHGDH) contain multiple cysteine residues. To determine the cysteine residue(s) responsible for the observed enzyme inhibition, a series of cysteine to serine variants were prepared to compare the k_{cat}/K_M values of the GSH versus GSNO treated samples. We anticipated that the activity of the cysteine to serine variant enzyme when treated with GSNO would be comparable to the GSH-treated enzyme. For 6PGD, residue C289 was identified in the Ischiropoulos study as *S*-nitrosated (23) and the variant C289S basal k_{cat}/K_M is 22% of wild type activity, which is indicative of the importance of this cysteine residue for maximal activity. It should be noted that nearly all the cysteine residues mutated are highly conserved in vertebrates (Figure S1), indicating these residues are important for function. Therefore, it is not surprising that the

untreated activity of these variants is lower that the activity of the wild type enzyme. However, the 6PGD variant C289S is still sensitive to GSNO treatment and therefore is likely not the *S*-nitrosated cysteine residue responsible for the activity decrease (Figure 2D). A complete series of variants was generated for the nine 6PGD cysteine residues (Figure S1A), where C289S was used as a background mutation so all other variants are double mutants (along with one triple mutant).

The 6PGD variants C199S/C289S and C289S/C422S could not be expressed as soluble protein. Cys170 and Cys171 are adjacent to each other in a buried loop, so the triple mutant of C170S/C171S/C289S was expressed and purified; however, this triple mutant was inactive. Of the remaining five 6PGD variant constructs (C30S/C289S, C113S/C289S, C289S, C289S/C366S and C289S/C402S), only 6PGD C289S/C366S activity was not significantly inhibited by *S*-nitrosation with a k_{cat}/K_M value of 0.037 $\mu M^{-1}s^{-1}$ for the GSH-treated negative control compared to the GSNO-treated k_{cat}/K_M value of 0.024 $\mu M^{-1}s^{-1}$ (Figure 2D). This represents 67% of GSH-treated activity for C289S/C366S compared to 0.8% activity for wild-type 6PGD. The activity of GSH-treated 6PGD C289S/C366S is low (6% compared to wild type), which can be attributed to the importance of C366 for activity; however, the k_{cat}/K_M value of the GSNO-treated 6PGD C289S/C366S is 650% that of the GSNO-treated WT enzyme.

Both C95 and C315 of ALDH4A1 displayed eNOS-dependent *S*-nitrosation in the Ischiropoulos study (23). We determined that the k_{cat}/K_M values for ALDH4A1 C95S were 0.26 (GSH treatment) and 0.017 $\mu M^{-1}s^{-1}$ (GSNO treatment), while the C315S variant exhibited k_{cat}/K_M values 0.037 and 0.0091 $\mu M^{-1}s^{-1}$ for GSH- and GSNO-treated samples, respectively (Figure 3D, Table 2). These results suggest that C315 has a greater effect on the inhibition of ALDH4A1 by *S*-nitrosation: GSNO-treated C315S exhibited 25% the activity of GSH-treated, whereas the C95S variant exhibited 6% activity of GSH-treated.

The Ischiropoulos study identified C241 in COMT as an *S*-nitrosated residue (23). This cysteine is located on the protein surface and distant from the active site. Treatment of COMT C241S with 150 μM GSNO resulted in inhibition similar to the inhibition observed with wild-type COMT (Figure 4D, Table 2), suggesting that C241 is not the residue responsible for GSNO-mediated inhibition. After surveying the COMT structure (PDB 3A7E), C223 was identified as a surface-exposed cysteine at the entrance to the active site: a potential location that could influence activity upon *S*-nitrosation (Figure 4A). The C223S variant was found to have k_{cat}/K_M values of 0.21 $\mu M^{-1}min^{-1}$ upon GSNO treatment compared to 0.36 $\mu M^{-1}min^{-1}$ for GSH-treated enzyme, corresponding to 59% activity upon GSNO treatment (Figure 4D, Table 2). The C223S variant was much less inhibited by GSNO treatment compared to wild-type COMT, which exhibited a 26% decrease in activity upon GSNO treatment.

An initial activity assay of the C281S variant in PHGDH, the residue identified in the Ischiropoulos proteomics study (23), exhibited 22% activity upon GSNO treatment, which is even more inhibited than wild-type PHGDH (Figure 5D, Table 2). A survey of the PHGDH crystal structure (PDB 2G76) identified four additional PHGDH cysteine residues that could affect enzymatic activity by either disrupting the active site or overall structure. Serine variants of each cysteine were generated and C116 was identified as the cysteine residue most affecting activity from GSNO treatment (Figure 5A). The k_{cat}/K_M value for GSNO-treated PHGDH C116S was 83% of GSH-treated enzyme, which is a small change compared to the 29% activity observed for GSNO-treated wild-type PHGDH (Figure 5D). C116 is found at the homodimer interface of PHGDH in a potential location to form a disulfide bond with C116 of the neighboring monomer. To the best of our knowledge, there is no evidence *in vivo* to suggest that PHGDH forms a disulfide, although *S*-nitrosation has been known to induce disulfide formation (39, 40). Therefore, it is possible that *S*-nitrosation of C116 induces disulfide formation, leading to a structural change that lowers the activity of PHGDH.

Percentage of S-nitrosation correlates with inhibition–To further evaluate the effect of *S*-

nitrosation on the identified cysteine residues and enzyme inhibition, 6PGD and ALDH4A1 were incubated with increasing GSNO concentrations (20–2000 μM) and the extent of *S*-nitrosation was analyzed with a D-switch assay (41). This LC-MS-based assay provides relative abundances of *S*-nitrosated and unmodified cysteine residues. COMT and PHGDH were not included because peptides containing essential cysteine residues were not detected during LC-MS analysis. It is expected that some free thiols are more reactive towards GSNO *in vitro* and the results here show that. The cysteine residues C366 in 6PGD and C315 in ALDH4A1, identified through mutagenesis as the likely sites of *S*-nitrosation, exhibited increasing levels of *S*-nitrosation with increasing concentrations of GSNO (Figures 2E and 3E). Other cysteine residues quantified in the D-switch assays, including C422 in 6PGD and C66 in ALDH4A1, were found mostly unmodified compared to other quantified cysteine residues. Still other cysteine residues, such as C113 in 6PGD, exhibited similar *S*-nitrosation efficiency as the targeted cysteine residues, but the activity differences from mutagenesis clearly demonstrated that these cysteine residues were not responsible for the observed enzyme inhibition upon GSNO treatment.

For comparison, the same GSNO treatments were used to test enzyme activity. Increasing GSNO concentrations correlated with decreasing activity for each enzyme, which corresponds to approximate *in vitro* GSNO IC_{50} values of 556 μM for 6PGD and 78 μM for ALDH4A1 (Figures 2F and 3F). These values are too large to be physiologically relevant compared to *in vivo* concentrations of GSNO (predicted to be in the low μM range). Since the exact physiological mechanism of *S*-nitrosation is unknown for these proteins, it is more relevant to correlate levels of *S*-nitrosation with activity. When comparing these IC_{50} values to the D-switch results, increasing *S*-nitrosation of C366 in 6PGD and C315 in ALDH4A1 clearly correlates with decreasing k_{cat}/K_M values (Figures 2E/F and 3E/F). This result, in conjunction with the mutagenesis data, indicates that these cysteine residues are responsible for the activity decreases observed upon GSNO treatment.

Discussion

S-nitrosation is difficult to study under physiological conditions due to the cysteine reactivity of •NO-derived nitrosating agents, low cellular •NO concentrations, and the indirect detection methods used for this posttranslational modification. In addition, varying levels of cysteine *S*-nitrosation will occur based on the relative reactivity of specific cysteine residues. Additionally, it remains unclear how *S*-nitrosation occurs enzymatically, as there are only a small number of known transnitrosating enzymes (17). Since it is known that *S*-nitrosation occurs *in vivo* (42), we focused on metabolic enzymes that are targets of *S*-nitrosation in which *S*-nitrosation modulates activity. To complement the Ischiropoulos *S*-nitrosation proteomics study (23), we performed metabolomics with wild-type and eNOS knockout mice to search for *S*-nitrosated metabolic enzymes with eNOS-dependent fluctuations in their substrate and product levels. This provided a list of 21 enzymes that are *S*-nitrosated and exhibited modulated substrate and product levels in an eNOS-dependent manner (Table S1). As both studies indicate, *S*-nitrosation abundance and metabolic effects are likely tissue-specific and this specificity needs to be further addressed in future studies. Of these 21 enzymes, we further characterized the effects of *S*-nitrosation on 6PGD, ALDH4A1, COMT, and PHGDH (Figures 2, 3, 4, and 5).

The transnitrosating agent GSNO was used to *S*-nitrosate each enzyme, but increasing concentrations of GSNO will eventually *S*-nitrosate all the accessible cysteine residues of a protein. In addition, inhibition of each enzyme was not necessarily due to the specific cysteine residue identified in the Ischiropoulos study (23). To relate enzyme inhibition to a specific cysteine residue, mutagenesis was performed and a range of GSNO concentrations were used to compare enzyme activity with the percent modification of each cysteine residue (23). Based on our experiments, C366 in 6PGD, C315 in ALDH4A1, C223 in COMT, and C116 in PHGDH appear to be the cysteine residues most responsible for the observed decrease in activity upon GSNO treatment. Apart from a study by Fox and coworkers, where an iNOS/S100A8/A9 complex was shown to *S*-

nitrosate cysteine residues in a [I/L]-X-C-X_2-[E/D] motif (16), no consensus sequence has been reported that predicts sites of cysteine *S*-nitrosation (35, 43). The cysteine residues identified in this study are also not part of any discernable consensus sequence. This is in contrast to other post-translational modifications such as phosphorylation, glycosylation or protease cleavage sites where conserved consensus sequences exist (44). While each cysteine identified here is conserved to varying degrees, these cysteine residues are mostly invariant in vertebrates and more variant in invertebrates (Figure S1). Since all vertebrates but only a subset of invertebrates encodes NOS isoforms, cysteine residues would be more likely to be targeted by *S*-nitrosation when the organism or host possesses a NOS homolog.

Of the four enzymes tested, 6PGD was most highly affected by *S*-nitrosation, exhibiting a decrease in k_{cat}/K_M by two orders of magnitude, while also requiring a higher GSNO concentration for inhibition (Figure 2D/F). Based on mutagenesis experiments and D-switch assays, C366 was identified as the residue most responsible for this significant activity change (Figure 2D/E). The C366S variant was the only variant tested in this study that lost sensitivity to GSNO (*i.e.* the activity was not significantly inhibited upon GSNO treatment). Additionally, *S*-nitrosation at C366 of the wild-type enzyme, as measured by a D-switch assay, correlated with a decrease in enzyme activity (Figure 2F). This strongly indicates that *S*-nitrosation of C366 is responsible for the observed inhibition of 6PGD upon GSNO treatment. Of all the residues identified in this study, C366 is the only cysteine residue that is highly conserved from mammals to bacteria, demonstrating the functional importance of this residue (Figure S1A). C366 is centered between the two half-domains of 6PGD and borders the active site pocket 6–8 Å away from the active-site catalytic and ligand-binding residues (Figure 2A). The hydroxyl side-chain of residues S129 and S140 are within hydrogen-bonding distance of the C366 thiol at 3.3 Å and 3.6 Å, respectively (Figure 2A), and their interactions may play a role in the structural orientation and rigidity of each half-domain. The changes in steric bulk and electrostatic potential that would occur upon *S*-nitrosation of C366 may disrupt this orientation and critical active site interactions, which would account for the GSNO-mediated decrease in activity.

While both C95 and C315 of ALDH4A1 were found to be *S*-nitrosated in the Ischiropoulos study (23), we found C315 was more responsible for inhibition, with C315S decreasing to 25% activity, upon *S*-nitrosation (Figure 3D). This change in activity is not as great as the 7% activity of wild-type and 6% activity of the C95S variant upon GSNO treatment. However, the 25% activity in C315S is still significant, suggesting additional cysteine residues contribute to *S*-nitrosation-derived inhibition. The residue C315 is highly conserved in animals, but is a threonine in most single-celled organisms, suggesting that C315 is important for proper protein function in multicellular organisms and may have evolved to mediate ALDH4A1 activity via *S*-nitrosation (Figure S1B). Similar to C366 of 6PGD, C315 of ALDH4A1 is located between two half domains at the periphery of the active site and borders the catalytic residue E314. *S*-Nitrosation of C315 could disrupt substrate binding to inhibit the enzyme (Figure 3A). Unlike 6PGD, the C315 side chain in ALDH4A1 borders a hydrophobic cleft and resides within a Van der Waals distance of 4–5 Å from F284, V288 and F291. *S*-nitrosation of this residue would likely disrupt a portion of the protein hydrophobic core as well as misalign the catalytic proton acceptor E314 and disrupt catalytic efficiency.

COMT treated with 150 μM GSNO exhibited 26% of the activity of GSH-treated COMT (Figure 4D). COMT activity was not detectable at higher GSNO concentrations. The C223 residue is highly conserved among vertebrates with a notable exception being it is a valine in mice (Figure S1C). Therefore, C223 could not be identified as a *S*-nitrosation target in the Ischiropoulos study (23), although it may be important for COMT regulation and activity in humans and other vertebrates. C223 is located on the protein surface, near the entrance to the active site pocket (Figure 4A). *S*-nitrosation could reduce ligand access to the active site due to increased steric bulk and modulated electrostatic potential on the surface. Since C223 is surface exposed, the solvent accessibility probably contributes to the increased sensitivity of C223 to GSNO treatment.

Of the four enzyme targets, PHGDH is the least sensitive to *S*-nitrosation, exhibiting 29% activity upon treatment with 2 mM GSNO. The C116S variant is largely unaffected by GSNO treatment and displays 83% of the GSH-treated activity (Figure 5D). While C116 is variable in invertebrates, C116 is highly conserved in vertebrates (Figure S1D) and is located at the surface, but on the opposite side from the PHGDH active site. Since the sequence of the *C*-terminal regulatory domain of human PHGDH indicates it is a type I PHGDH enzyme, it is predicted to form a tetramer *in vivo* (45). Although the construct used in this study does not include the *C*-terminal domain, it could likely dimerize; the crystal structure of human PHGDH, which is also lacking the *C*-terminal domain, also forms a dimer (PDB 2G76). Residue C116 is located at the putative dimer interface and the thiol side chain is oriented 3.3 Å away from C116 of the dimer partner (Figure 5A). Therefore, *S*-nitrosation of C116 may either disrupt dimerization of PHGDH or induce an *S*-nitrosation-derived disulfide. Disulfide formation and generation of nitroxide (NO^-) as a consequence of *S*-nitrosation has been demonstrated in a few cases (39, 40, 46). A disulfide bond could force the enzyme to adopt a more rigid conformation, resulting in GSNO-mediated inhibition. However, the exact mechanism requires further investigation.

Using a metabolomics approach to prioritize metabolic enzymes for further study, we demonstrated that four important metabolic enzymes (6PGD, ALDH4A1, COMT, and PHGDH) are inhibited by GSNO transnitrosation *in vitro*. These results demonstrate that *S*-nitrosation of C366 of 6PGD, C315 of ALDH4A1, C223 of COMT, and C116 of PHGDH inhibit enzyme activity. Although the enzymes ALDOA and TPI-1 were identified to be *S*-nitrosated in the proteomics study (23) as well as the TAMRA-maleimide-switch assay (Figure 6A), the metabolomics data did not suggest that ALDOA or TPI-1 would be inhibited by *S*-nitrosation and were unaffected by GSNO treatment as anticipated. While the concentrations of GSNO required for enzyme inhibition are higher than physiological levels (low µM range *in vivo*), •NO and GSNO may reach higher local concentrations proximal to NOS. Additionally, other •NO-derived agents and proteins may convey *S*-nitrosation specificity. Since the physiological mechanism of *S*-nitrosation is unclear for the metabolic enzymes studied herein, varying GSNO concentrations were used to *S*-nitrosate the cysteine residues that affect activity. In this case, modifying the correct cysteine residues to observe inhibition was more important than the non-specific modifications of cysteine residues at higher concentrations of GSNO that had less of an inhibitory affect. This study highlights a novel strategy to identify physiologically relevant targets of *S*-nitrosation with an emphasis on functional effects of *S*-nitrosation of metabolic enzymes. The synergistic analysis of proteomics and metabolomics data was successful in identifying four functionally modulated *S*-nitrosated enzymes. The remaining 17 metabolic enzymes identified in this study as potentially regulated by *S*-nitrosation await further characterization.

Experimental procedures

Metabolomics. Adult *B6.129P2-Nos3*^{tm1Unc}*/J* (*eNOS*$^{-/-}$) C57BL/6J mice (Jax cat# 002684) were purchased from Jackson Laboratories (Bar Harbor, ME). Age-matched wild-type C57BL/6J mice were bred in an AAALAC-approved facility at the Scripps Research Institute. All procedures followed the guidelines of the Institutional Animal Care and Use Committee (IACUC) of the Scripps Research Institute. Animal housing followed a typical 6 AM/6 PM light/dark phase with free access to water and food. Six sets of both wild-type and *eNOS*$^{-/-}$ mouse brain, heart, kidney, liver, lung and pancreas were harvested, flash frozen in liquid N_2, and stored at –80 °C until further processing. The organs were extracted by the Scripps Center for Metabolomics and Mass Spectrometry, as previously described (47, 48). LC-MS analysis of each sample was performed at the Scripps Center for Metabolomics and Mass Spectrometry using negative and positive mode MS for the C18 column and negative mode MS for the HILIC column. Resulting MS spectra and LC peak integrations were collected and analyzed using XCMS Online (27-29).

Proteomics and metabolomics analysis. Proteomic data was taken from the supplemental materials of Doulias *et al.* (23) and rearranged to identify each enzyme with eNOS dependent *S*-nitrosation. From this list, less than 10% of identified cysteine

residues had an annotated function as either a catalytic, ligand/metal-binding, post-translationally modified, disulfide or protein-protein interaction residue. For metabolomics analysis, XCMS Online and METLIN analysis for each organ (n = 6) only utilized MS peaks with $p < 0.1$ when comparing differences between wild-type and *eNOS*$^{-/-}$ data (27, 30, 48). The average integrated peak area for each mass feature was compiled into tables, with separate tables for negative (C18 and HILIC) and positive (C18 only) mode MS analysis for each organ. Worksheets for each organ and ionization mode were uploaded to Pathos online to compare wild-type and *eNOS*$^{-/-}$ metabolomes (32). The combination of differences from all organs for each metabolite was plotted onto KEGG metabolic pathway maps with minimal difference in mean mass feature integrations between wild-type and *eNOS*$^{-/-}$ organs of 1.4-fold used in the analysis (31, 49, 50). Metabolic enzymes showing eNOS-dependent *S*-nitrosation from the Ischiropoulos proteomics study (23) were then added to the KEGG maps. *S*-nitrosated enzymes with metabolomic mass features matching increased product and decreased substrate (or decreased product and increased substrate) levels in *eNOS*$^{-/-}$ compared to WT mice were compiled to generate an initial enzyme targets list (Table 1). Targets were further narrowed based on criteria outlined in the Results section to identify 21 enzymes (Table S1), including four for *in vitro* testing: 6PGD, ALDH4A1, COMT and PHGDH.

Subcloning. Human ALDOA (Uniprot ID P04075) in a pMCSG7 expression vector (AmpR) with a *N*-terminal 6× His tag and Tobacco Etch Virus (TEV) cleavage site was ordered from Harvard PlasmID repository (Clone ID HsCD00286766). An intron was removed from the construct using a standard site-directed mutagenesis loop excision protocol with primers in Table S2. DNA encoding human genes of 6PGD (Uniprot ID P52209), ALDH4A1 (Uniprot ID P30038), COMT (Uniprot ID P21964), PHGDH (Uniprot ID O43175), and TPI1 (Uniprot ID P60174) were obtained from Harvard PlasmID repository with ID's HSCD00438431, HSCD00331467, HSCD00324442, HSCD00322318, and HSCD00042264, respectively.

Two methods of subcloning were utilized for the remaining enzyme targets, separated by method:

Gateway cloning. COMT (pDONR221 to pDEST42, C-His), PHGDH (pDONR221 to pDEST527, N-His), and TPI-1 (pDONR221 to pDEST42, C-His) were cloned utilizing Gateway cloning methods (51). Both constructs were initially cloned into pDONR221 with BP Clonase II. After purification, transformation and mini-prepping pDONR221 constructs, each construct was transferred to their respective destination vectors utilizing LR Clonase II reaction.

The soluble isoform of COMT was used for domain boundaries, excluding the first 50 amino acids that are present in membrane-bound COMT. The final construct ranged from M51 to P271 and was cloned into pDEST42 with a C-terminal V5 epitope and 6× His tag. PHGDH domain boundaries were chosen based on the published crystal structure (PDB ID: 2G76), which lacks the regulatory C-terminal domain and ranges from M1 to V315, and was cloned into pDEST527 with a N-terminal 6× His tag. These domain boundaries were chosen because full-length PHGDH was found to be largely insoluble.

Golden Gate cloning. 6PGD and ALDH4A1 were cloned utilizing a Golden Gate cloning method into a pET28-GG vector (kindly provided by the Tullman-Ercek lab) using constructs with N-terminal 6× His tags and TEV protease cleavage sites for each (52). Since the 6PGD *N*-terminal methionine is removed *in vivo*, the domain boundaries for this construct were from A2 to A483. ALDH4A1 contains a signal sequence on the *N*-terminus that is removed *in vivo* and this signal sequence was not included in the construct to give domain boundaries from T18 to Q563.

Site-directed mutagenesis. Sequence and cysteine numbering is based on the human enzyme. Primers were obtained from Sigma-Aldrich or Integrated DNA Technologies (Table S2). Mutagenesis was accomplished through PCR and sequences were confirmed using standard Sanger sequencing by GeneWiz or the UC-Berkeley sequencing facility. Site-directed mutants were transformed into BL21(DE3) *E. coli* and purified similarly to their respective wild-type constructs as detailed below.

Enzyme expression and purification. Each construct was transformed into BL21(DE3) *E. coli* and inoculated with 2 mL of a 6 mL overnight culture into 1 L terrific broth plus appropriate antibiotic. Cells were grown to $OD_{600\ nm}$ = 0.4-0.6. ALDOA, TPI1, and COMT (and cysteine variants) were induced with 1 mM IPTG at 37 °C for 4 h. The enzymes 6PGD, ALDH4A1, and PHGDH along with their variants were incubated on ice for 15 min and induced with 0.7 mM IPTG overnight at 18 °C. Cell pellets were obtained by centrifugation at 4000 rpm for 15 min at 4 °C. Pellets were washed with 20 mM Tris, pH 8.0, pelleted once more, flash frozen in liquid nitrogen and stored at –80 °C until purification. Frozen cell pellets were thawed quickly in room temperature water, resuspended in ice cold lysis buffer (50 mM Tris-HCl at pH 8.0, 300 mM NaCl, 10% v/v glycerol and 10 mM imidazole) supplemented with 0.25 mg/mL lysozyme, 20 µg/mL DNaseI and 20 µg/mL benzamidine. Resuspended cells were stirred at 4 °C for 30 min and sonicated to break cells (5 min with 2 s on, 4 s off). Cell debris was removed by centrifugation (35,000 rpm for 35 min or 15,000 rpm for 1 h) and the supernatant was mixed with ClonTech His60 nickel (Ni) resin pre-equilibrated in lysis buffer. The Ni resin slurry was stirred for 45 min to 2 h. Unbound proteins were removed by application of the resin to a gravity column and the flow-through was reapplied to the Ni. The Ni resin was then washed with ten column volumes of lysis buffer. Bound protein was eluted with increasing concentrations of imidazole in lysis buffer (40 to 450 mM). Most protein eluted between 100 and 250 mM imidazole. Purity of the eluted fractions was confirmed by SDS-PAGE using Bio-Rad Stain-Free methods; fractions containing the desired protein were combined and concentrated with 10 kDa molecular weight cut-off (MWCO) spin concentrators in a Beckman Coulter Allegra X-14R centrifuge at 4 °C at 3,000-4,000 rcf. ALDH4A1 was further purified with anion-exchange chromatography with a POROS HQ20 column using a 0-100% buffer B in buffer A gradient (Buffer A: 100 mM Tris-HCl at pH 8.0, 10% v/v glycerol, 2 mM DTT, 5 mM EDTA. Buffer B: Buffer A plus 1 M NaCl). The enzymes 6PGD and ALDH4A1 were further purified by size exclusion chromatography with a GE HiLoad 26/600 Superdex 200 column pre-equilibrated in freezing buffer (50 mM Tris-HCl at pH 8.0, 50 mM NaCl, 5% v/v glycerol, 1 mM EDTA and 1 mM DTT) and COMT was further purified with a GE HiLoad 16/600 Superdex 75 column pre-equilibrated in freezing buffer. The purest fractions, as assessed by SDS-PAGE, were combined. ALDOA, PHGDH and TPI1 were buffer exchanged into freezing buffer with a PD-10 column. All proteins were concentrated to 10-20 mg/mL, flash frozen in liquid nitrogen, and stored at –80 °C.

S-nitrosation of purified enzymes. Frozen protein aliquots were thawed on ice. Proteins were diluted to 150 µL in the appropriate activity buffer (see "Enzyme activity assays" subsection), reduced with 2 mM TCEP for 20-30 min and then buffer exchanged into appropriate activity buffers using Bio-Rad Bio-Spin6 columns. Protein concentrations were determined by Bradford assay or the absorbance at 280 nm (using molar extinction coefficients of 63.4 $mM^{-1}cm^{-1}$ for 6PGD, 74.3 $mM^{-1}cm^{-1}$ for ALDH4A1, 22.9 $mM^{-1}cm^{-1}$ for COMT and 13.9 $mM^{-1}cm^{-1}$ for PHGDH). GSNO stock concentrations were measured before use ($\varepsilon_{335\ nm}$ = 0.992 $mM^{-1}cm^{-1}$). All proteins, except PHGDH, were incubated separately at 20 µM with varying GSNO or GSH concentrations (20, 50, 100, 150, 200, 500, 1000 or 2000 µM) at 37 °C for 1 h. PHGDH was incubated at 150 µM with GSNO or GSH concentrations of 150, 500, 1000 or 2000 µM for 1 h. For kinetics experiments, 6PGD and PHGDH were incubated with 2 mM GSH or GSNO for 1 h at 37 ˚C, ALDH4A1, ALDOA, and TPI1 were incubated with 1 mM GSH or GSNO for 1 h at 37˚C and COMT was incubated for 150 µM GSH or GSNO for 1 h at 37 ˚C. Proteins were spun at ~21,000 rcf for 1 min to remove precipitation and the supernatant was buffer exchanged into the appropriate activity buffer using Bio-Spin6 columns. Protein concentrations were measured and diluted with activity buffer to stock solutions of 1 µM for 6PGD, ALDH4A1, TPI1 and ALDOA; 10 µM for COMT; or 50 µM for PHGDH.

TAMRA-maleimide switch assay. Each enzyme was diluted to 100-400 µM in HEN buffer (250 mM HEPES at pH 7.7, 1 mM EDTA, and 0.1 mM neocuproine) and reduced with 3 mM TCEP for 20 min at room temperature. Enzymes were then exchanged into HEN buffer with pre-equilibrated Bio-Rad Spin6 columns to remove excess TCEP. A 50 µL aliquot of 20 µM enzyme and 100-2000 µM

GSNO or GSH were incubated at 37 °C for 1 h. Reactions were quenched with an equal volume of cysteine blocking buffer (6 M Urea, 200 mM iodoacetamide, and 1% w/v SDS in HEN) and incubated for 1 h at 37 °C. Protein was precipitated with 1 mL of cold acetone (stored at –20 °C), thoroughly mixed and pelleted at 21,000 rcf for 10 min at 4 °C and supernatant was removed and discarded. This acetone precipitation was repeated 1-2 more times to remove all the blocking buffer and then incubated at 37 ˚C for 10-20 min after the final supernatant removal to evaporate any residual acetone. Pellets were resuspended in labeling buffer (6 M urea, 60 mM ascorbate, and 200 µM tetramethylrhodamine (TAMRA) maleimide diluted in PBS) and incubated at 37 °C for 1 h. Samples were analyzed by SDS-PAGE and washed with destain buffer (40% v/v methanol and 10% v/v acetic acid) 3 times for at least 20 min each followed by rehydration in MilliQ H_2O before TAMRA imaging on a Bio-Rad ChemiDoc to confirm that the enzymes were modified, followed by Coomassie staining to demonstrate equal protein loading.

Enzyme activity assays. To determine k_{cat} and K_M values, eight substrate concentrations were used for each protein and variant. All substrates, cofactors and enzymes were dissolved or exchanged into buffers specific for each assay, as described below. Product formation for all proteins (except COMT) was continuously monitored by absorbance changes at 340 nm over a period of 5 to 10 min. Initial rates were determined from the least-square fit of the linear portion of substrate turnover. COMT was assayed using a discontinuous HPLC-based end-point assay as described below. Initial rates were plotted versus substrate concentration using GraphPad Prism and fitted using non-linear regression to the Michaelis-Menten equation to determine k_{cat} and K_M values.

6PGD assay: The activity assay buffer was comprised of 100 mM HEPES at pH 7.5, 50 mM KCl and 1 mM EDTA. The assay mixture contained 200 µM $NADP^+$ and varying concentrations of 6-phosphogluconate (5, 10, 25, 50, 75, 100, 250 or 500 µM); the assay was initiated by the addition of 20 nM 6PGD. For 6PGD GSNO-treated samples, the assay was initiated with 600 nM enzyme.

ALDH4A1 assay: This assay first required the synthesis of the substrate L-Δ^1-pyrroline-5-carboxylate:

Synthesis of L-Δ^1-pyrroline-5-carboxylate: L-Δ^1-pyrroline-5-carboxylate was synthesized as previously described (53, 54). All steps were performed on ice. Briefly, 3.1 mL of 50 mM sodium periodate (pH to 7.0 with 1 M NaOH) was added to 2 mL of 70 mM DL-5-hydroxylysine hydrochloride and incubated for 8 min. Glycerol (50 µL of 1 M) was added and incubated for 2 min to quench the periodate. Then, 45 µL of 6 M HCl was added to acidify the reaction. L-Δ^1-pyrroline-5-carboxylate was purified using Bio-Rad AG1-X8 resin in a 2×30 cm column treated with 1.0 M HCl before washing with 4 column volumes of MilliQ water. The reaction mixture was added to the column, washed with 1 column volume of 50 mM HCl and eluted with 1 M HCl, collecting 1 mL fractions. Fractions containing L-Δ^1-pyrroline-5-carboxylate were identified by mixing aliquots with 0.5% *o*-aminobenzaldehyde in ethanol and monitoring the absorbance at 444 nm. Fractions containing L-Δ^1-pyrroline-5-carboxylate were combined and the concentrations were noted before storage at –80 °C.

ALDH4A1 assay: The activity assay buffer was comprised of 100 mM HEPES at pH 8.1, 50 mM KCl and 1 mM EDTA. The assay mixture contained 300 µM NAD^+ with varying concentrations of L-Δ^1-pyrroline-5-carboxylate (5, 10, 15, 25, 50, 75, 100 or 200 µM); the assay was initiated by addition of 20 nM ALDH4A1.

COMT assay: The activity assay buffer was 100 mM sodium phosphate at pH 7.6 and 1.2 mM $MgCl_2$. The assay mixture contained 1 mM SAM with varying concentrations 3,4-dihydroxybenzoic acid (DHBA) (5, 10, 15, 20, 40, 60 or 100 µM) and was pre-incubated for 2-3 min at 37 °C before enzyme addition. The assay was initiated by the addition of 200 nM COMT in a 450 µL Eppendorf tube and incubated at 37 °C. For each time point (0, 2, 4 and 6 min for 5, 15 and 20 µM DHBA; 0, 3, 6 and 9 min for 40, 60 and 100 µM DHBA), 100 µL aliquots were removed and quickly mixed with 15 µL 60% w/v perchloric acid to quench the reaction. Quenched reaction aliquots were stored at –80 °C until HPLC analysis. Aliquots were thawed and centrifuged at 21,000 rcf for 5 min at 4 °C. The

supernatant was transferred to an HPLC vial and 100 µL of the sample was injected onto a C18 reverse phase column (Agilent Eclipse Plus XDB C18 4.6×100 mm 3.5 µm particle size, 80 Å pore size) with an Agilent 1260 Infinity HPLC system. A gradient consisting of two buffers (buffer A: 0.1% v/v formic acid in MilliQ filtered water and buffer B: 99.9% v/v acetonitrile with 0.1% v/v formic acid) was used with the following conditions: 5% B for 0-5 min, 5-17% B for 5-20 min, 17-100% B for 20-21 min, 100% B for 21-26 min, 100-5% B for 26-27 min and 5% B for 27-34 min. The absorbance of the substrate (DHBA) and product (vanillic and isovanillic acid) peaks was monitored at 260 nm. Concentrations of vanillic and isovanillic acid were determined by plotting a standard curve using standards obtained from Sigma-Aldrich. Rates were determined from vanillic acid production as it is produced in approximately 5:1 ratio compared to isovanillic acid.

PHGDH assay: The activity assay buffer was comprised of 200 mM HEPES at pH 7.5, 50 mM KCl and 1 mM EDTA. The assay mixture contained 1 µM PHGDH with varying concentrations of oxaloacetate (OAA) (0.2, 0.5, 1, 5, 10, 15, 20 or 40 mM); the assay was initiated by addition of 200 µM NADH. Since higher concentrations of OAA (> 20 mM) absorb at 340 nm and slowly oxidize NADH, a control without enzyme was used to account for the background reactivity of the substrate. To minimize decomposition, OAA was dissolved in the activity assay buffer immediately before use.

ALDOA assay: The activity assay buffer was comprised of 100 mM HEPES at pH 7.5, 50 mM KCl and 1 mM EDTA. The assay mixture contained 200 µM NADH, 2 mU/µL GPDH/TPI (α-Glycerophosphate dehydrogenase/Triosephosphate isomerase) enzyme mixture from Sigma-Aldrich with varying concentrations of fructose-1,6-bisphosphate (2, 5, 10, 20, 50, 100, 250 or 500 µM); the assay was initiated by the addition of 50 nM ALDOA.

TPI1 assay: The activity assay buffer was comprised of 100 mM HEPES at pH 7.5, 50 mM KCl and 1 mM EDTA. The assay mixture contained 200 µM NADH, 2 mU/µL GPDH (α-Glycerophosphate dehydrogenase) from Sigma-Aldrich with varying concentrations of glyceraldehyde-3-phosphate (0.05, 0.1, 0.2, 0.5, 1, 2, 4 or 8 mM); the assay was initiated by the addition of 0.2 nM TPI1.

D-switch assay. 6PGD and ALDH4A1 were analyzed by a D-switch assay (41). After 20 µM enzyme was incubated with various GSNO concentrations for 1-2 h, as described above for the TAMRA-switch assay, an equal volume of blocking buffer [50 mM *N*-ethylmaleimide (NEM), 7 M urea and 1% w/v SDS dissolved in HEN Buffer (100 mM HEPES at pH 7.5, 1 mM EDTA and 0.1 mM neocuproine)] was added to each reaction and sonicated in a water bath for 5 min. Samples were then incubated for 1 h at 55 °C. Protein was precipitated by the addition of 1 mL of cold acetone (stored at –20 °C) followed by 10 min incubation at –80 °C and centrifugation at 21,000 rcf for 10 min at 4 °C. The supernatant was gently removed and the pellet was resuspended in 1 mL of cold acetone one or two more times, until the pellets were white and all of the buffer was exchanged. Residual acetone was removed by incubating samples for a few minutes at 37 °C before adding 5 mM d_5-NEM dissolved in HBS (100 mM HEPES at pH 7.2 and 150 mM NaCl) with 7 M urea and 30 mM sodium ascorbate and incubating 1 h at 37 °C. Samples were diluted 14× in HBS plus 5 mM $CaCl_2$ and protein was digested overnight while shaking at 37 °C with chymotrypsin for 6PGD or trypsin/LysC for ALDH4A1. Samples were pelleted at 21,000 rcf for 5 min at room temperature to remove any precipitate and the supernatant was transferred to a new Eppendorf tube. Samples were analyzed by LC-MS and peaks of peptides containing cysteine residues were integrated and compared to determine the relative amounts of NEM and d_5-NEM labeled peptides.

Acknowledgements

This work was funded in part by the George E. Hewitt Foundation for Medical Research (J. J. B.), a National Institutes of Health National Institute of General Medical Sciences Postdoctoral Fellowship 5F32GM095023 (B. C. S.), and an American Heart Association Scientist Development Grant 15SDG25830057 (B. C. S.). We thank Bill Webb at the Scripps Center for Metabolomics and Mass

Spectrometry for assistance with metabolomics sample preparation and LC-MS analysis. We thank Kim Masuda for assistance with harvesting mouse organs and the Cravatt laboratory for generously donating the wild-type mice. We thank the QB3 MS facility at UC Berkeley, especially Anthony T. Iavarone. We thank the Marletta laboratory for helpful input.

Conflict of interest

The authors declare that they have no conflicts of interest with the contents of this article.

Author contributions

J. J. B. analyzed and combined proteomics and metabolomics data, subcloned all enzymes except ALDOA and TPI1, expressed and purified all enzymes, performed site-directed mutagenesis on all constructs, conducted *S*-nitrosation reactions and performed TAMRA-maleimide switch on all enzymes, performed and analyzed all enzyme activity assays, and performed and analyzed D-switch assays. S. L. W.-S. subcloned ALDOA and TPI1. S. L. W.-S and B. C. S. initiated and prepared mouse organs for metabolomics. J. J. B., S. L. W.-S., B. C. S., and M. A. M. conceived and designed the experiments, prepared figures and wrote the manuscript. M. A. M. acquired funding and coordinated the study. All authors reviewed the results and approved the final version of the manuscript.

References

1. Friebe, A., and Koesling, D. (2009) The function of NO-sensitive guanylyl cyclase: what we can learn from genetic mouse models. *Nitric Oxide*. **21**, 149–156
2. Liu, V. W. T., and Huang, P. L. (2008) Cardiovascular roles of nitric oxide: a review of insights from nitric oxide synthase gene disrupted mice. *Cardiovascular Research*. **77**, 19–29
3. Zhou, L., and Zhu, D. Y. (2009) Neuronal nitric oxide synthase: structure, subcellular localization, regulation, and clinical implications. *Nitric Oxide*. **20**, 223–230
4. Förstermann, U., and Sessa, W. C. (2012) Nitric oxide synthases: regulation and function. *European Heart Journal*. **33**, 829–837
5. Serafim, RAM, Primi, M., Trossini, G., and Ferreira, E. I. (2012) Nitric oxide: state of the art in drug design. *Curr. Med. Chem.* **19**, 386–405
6. Derbyshire, E. R., and Marletta, M. A. (2012) Structure and regulation of soluble guanylate cyclase. *Annu. Rev. Biochem.* **81**, 533–559
7. Hess, D. T., Matsumoto, A., Kim, S.O., Marshall, H. E., and Stamler, J. S. (2005) Protein *S*-nitrosylation: purview and parameters. *Nat. Rev. Mol. Cell Biol*. **6**, 150–166
8. Anand, P., and Stamler, J. S. (2012) Enzymatic mechanisms regulating protein *S*-nitrosylation: implications in health and disease. *J. Mol. Med*. **90**, 233–244
9. Yang, L., Calay, E. S., Fan, J., Arduini, A., Kunz, R. C., Gygi, S. P., Yalcin, A., Fu, S., and Hotamisligil, G. S. (2015) Metabolism. *S*-nitrosylation links obesity-associated inflammation to endoplasmic reticulum dysfunction. *Science*. **349**, 500–506
10. Nakamura, T., and Lipton, S. A. (2016) Protein *S*-nitrosylation as a therapeutic target for neurodegenerative diseases. *Trends Pharmacol. Sci.* **37**, 73–84
11. Huang, B., Chen, S. C., and Wang, D. L. (2009) Shear flow increases S-nitrosylation of proteins in endothelial cells. *Cardiovascular Research*. **83**, 536–546
12. Wynia-Smith, S. L., and Smith, B. C. (2016) Nitrosothiol formation and *S*-nitrosation signaling through nitric oxide synthases. *Nitric Oxide*. **63**, 52–60
13. Venerando, A., Cesaro, L., and Pinna, L. A. (2017) From phosphoproteins to phosphoproteomes: a historical account. *FEBS J.* **284**, 1936–1951
14. Mitchell, D. A., and Marletta, M. A. (2005) Thioredoxin catalyzes the *S*-nitrosation of the caspase-3 active site cysteine. *Nat. Chem. Biol*. **1**, 154–158
15. Jia, J., Arif, A., Willard, B., Smith, J. D., Stuehr, D. J., Hazen, S. L., and Fox, P. L.

(2012) Protection of extraribosomal RPL13a by GAPDH and dysregulation by *S*-nitrosylation. *Molecular Cell*. **47**, 656–663

16. Jia, J., Arif, A., Terenzi, F., Willard, B., Plow, E. F., Hazen, S. L., and Fox, P. L. (2014) Target-selective protein *S*-nitrosylation by sequence motif recognition. *Cell*. **159**, 623–634
17. Nakamura, T., and Lipton, S. A. (2013) Emerging role of protein-protein transnitrosylation in cell signaling pathways. *Antioxidants & Redox Signaling*. **18**, 239–249
18. Smith, B. C., and Marletta, M. A. (2012) Mechanisms of *S*-nitrosothiol formation and selectivity in nitric oxide signaling. *Current Opinion in Chemical Biology*. **16**, 498–506
19. Broniowska, K. A., and Hogg, N. (2012) The chemical biology of *S*-nitrosothiols. *Antioxidants & Redox Signaling*. **17**, 969–980
20. Lim, C. H., Dedon, P. C., and Deen, W. M. (2008) Kinetic analysis of intracellular concentrations of reactive nitrogen species. *Chem. Res. Toxicol.* **21**, 2134–2147
21. Yang, X., Bondonno, C. P., Indrawan, A., Hodgson, J. M., and Croft, K. D. (2013) An improved mass spectrometry-based measurement of NO metabolites in biological fluids. *Free Radical Biology and Medicine*. **56**, 1–8
22. Tsikas, D. (2012) Potential problems and pitfalls with the use of *S*-nitrosoglutathione and other *S*-nitrosothiols in physiology-oriented basic science. *The Journal of Physiology*. **590**, 6247–6248
23. Doulias, P. T., Tenopoulou, M., Greene, J. L., Raju, K., and Ischiropoulos, H. (2013) Nitric oxide regulates mitochondrial fatty acid metabolism through reversible protein *S*-nitrosylation. *Sci. Signal*. **6**, 1–7
24. Hara, M. R., Agrawal, N., Kim, S. F., Cascio, M. B., Fujimuro, M., Ozeki, Y., Takahashi, M., Cheah, J. H., Tankou, S. K., Hester, L. D., Ferris, C. D., Hayward, S. D., Snyder, S. H., and Sawa, A. (2005) *S*-nitrosylated GAPDH initiates apoptotic cell death by nuclear translocation following Siah1 binding. *Nature Cell Biology*. **7**, 665–674
25. Kolesnik, B., Palten, K., Schrammel, A., Stessel, H., Schmidt, K., Mayer, B., and Gorren, A. C. F. (2013) Efficient nitrosation of glutathione by nitric oxide. *Free Radical Biology and Medicine*. **63**, 51–64
26. Broniowska, K. A., Diers, A. R., and Hogg, N. (2013) *S*-nitrosoglutathione. *Biochim. Biophys. Acta*. **1830**, 3173–3181
27. Smith, C. A., Want, E. J., O'Maille, G., Abagyan, R., and Siuzdak, G. (2006) XCMS: Processing Mass Spectrometry Data for Metabolite Profiling Using Nonlinear Peak Alignment, Matching, and Identification. *Analytical Chemistry*. **78**, 779–787
28. Tautenhahn, R., Patti, G. J., Rinehart, D., and Siuzdak, G. (2012) XCMS Online: a web-based platform to process untargeted metabolomic data. *Analytical Chemistry*. **84**, 5035–5039
29. Gowda, H., Ivanisevic, J., Johnson, C. H., Kurczy, M. E., Benton, H. P., Rinehart, D., Nguyen, T., Ray, J., Kuehl, J., Arevalo, B., Westenskow, P. D., Wang, J., Arkin, A. P., Deutschbauer, A. M., Patti, G. J., and Siuzdak, G. (2014) Interactive XCMS Online: simplifying advanced metabolomic data processing and subsequent statistical analyses. *Analytical Chemistry*. **86**, 6931–6939
30. Smith, C. A., Maille, G. O., Want, E. J., Qin, C., Trauger, S. A., Brandon, T. R., Custodio, D. E., Abagyan, R., and Siuzdak, G. (2005) METLIN: a metabolite mass spectral database. *Therapeutic Drug Monitoring*. **27**, 747
31. Kanehisa, M., Araki, M., Goto, S., Hattori, M., Hirakawa, M., Itoh, M., Katayama, T., Kawashima, S., Okuda, S., Tokimatsu, T., and Yamanishi, Y. (2008) KEGG for linking genomes to life and the environment. *Nucleic Acids Research*. **36**, D480–484
32. Leader, D. P., Burgess, K., Creek, D., and Barrett, M. P. (2011) Pathos: a web facility that uses metabolic maps to display experimental changes in metabolites identified by mass spectrometry. *Rapid Commun. Mass Spectrom.* **25**, 3422–3426

33. Albery, W. J., and Knowles, J. R. (1976) Free-energy profile for the reaction catalyzed by triosephosphate isomerase. *Biochemistry*. **15**, 5627–5631
34. Tolan, D. R., Niclas, J., Bruce, B. D., and Lebo, R. V. (1987) Evolutionary implications of the human aldolase-A, -B, -C, and -pseudogene chromosome locations. *Am. J. Hum. Genet.* **41**, 907–924
35. Marino, S. M., and Gladyshev, V. N. (2010) Structural analysis of cysteine *S*-nitrosylation: a modified acid-based motif and the emerging role of trans-nitrosylation. *Journal of Molecular Biology*. **395**, 844–859
36. Derakhshan, B., Hao, G., and Gross, S. S. (2007) Balancing reactivity against selectivity: the evolution of protein S-nitrosylation as an effector of cell signaling by nitric oxide. *Cardiovascular Research*. **75**, 210–219
37. Forrester, M. T., Foster, M. W., Benhar, M., and Stamler, J. S. (2009) Detection of protein *S*-nitrosylation with the biotin-switch technique. *Free Radical Biology and Medicine*. **46**, 119–126
38. Jaffrey, S. R., Erdjument-Bromage, H., Ferris, C. D., Tempst, P., and Snyder, S. H. (2001) Protein *S*-nitrosylation: a physiological signal for neuronal nitric oxide. *Nature Cell Biology*. **3**, 193–197
39. Wang, Y. T., Piyankarage, S. C., Williams, D. L., and Thatcher, G. R. J. (2014) Proteomic profiling of nitrosative stress: protein *S*-oxidation accompanies *S*-nitrosylation. *ACS Chem. Biol.* **9**, 821–830
40. O'Brian, C. A., and Chu, F. (2005) Post-translational disulfide modifications in cell signaling--role of inter-protein, intra-protein, *S*-glutathionyl, and *S*-cysteaminyl disulfide modifications in signal transmission. *Free Radic. Res.* **39**, 471–480
41. Sinha, V., Wijewickrama, G. T., Chandrasena, R. E. P., Xu, H., Edirisinghe, P. D., Schiefer, I. T., and Thatcher, G. R. J. (2010) Proteomic and mass spectroscopic quantitation of protein *S*-nitrosation differentiates NO-donors. *ACS Chem. Biol.* **5**, 667–680
42. Maron, B. A., Tang, S.S., and Loscalzo, J. (2013) *S*-nitrosothiols and the *S*-nitrosoproteome of the cardiovascular system. *Antioxidants & Redox Signaling*. **18**, 270–287
43. Gould, N. S., Evans, P., Martínez-Acedo, P., Marino, S. M., Gladyshev, V. N., Carroll, K. S., and Ischiropoulos, H. (2015) Site-specific proteomic mapping identifies selectively modified regulatory cysteine residues in functionally distinct protein networks. *Chemistry & Biology*. **22**, 965–975
44. Blom, N., Sicheritz-Pontén, T., Gupta, R., Gammeltoft, S., and Brunak, S. (2004) Prediction of post-translational glycosylation and phosphorylation of proteins from the amino acid sequence. *Proteomics*. **4**, 1633–1649
45. Mattaini, K. R., Brignole, E. J., Kini, M., Davidson, S. M., Fiske, B. P., Drennan, C. L., and Vander Heiden, M. G. (2015) An epitope tag alters phosphoglycerate dehydrogenase structure and impairs ability to support cell proliferation. *Cancer Metab.* **3**, 1-12
46. Keszler, A., Zhang, Y., and Hogg, N. (2010) Reaction between nitric oxide, glutathione, and oxygen in the presence and absence of protein: How are *S*-nitrosothiols formed? *Free Radical Biology and Medicine*. **48**, 55–64
47. Ivanisevic, J., Zhu, Z.J., Plate, L., Tautenhahn, R., Chen, S., O'Brien, P. J., Johnson, C. H., Marletta, M. A., Patti, G. J., and Siuzdak, G. (2013) Toward 'omic scale metabolite profiling: a dual separation-mass spectrometry approach for coverage of lipid and central carbon metabolism. *Analytical Chemistry*. **85**, 6876–6884
48. Ivanisevic, J., Epstein, A. A., Kurczy, M. E., Benton, P. H., Uritboonthai, W., Fox, H. S., Boska, M. D., Gendelman, H. E., and Siuzdak, G. (2014) Brain region mapping using global metabolomics. *Chemistry & Biology*. **21**, 1575–1584
49. Kanehisa, M., and Goto, S. (2000) KEGG: kyoto encyclopedia of genes and genomes. *Nucleic Acids Research*. **28**, 27–30
50. Kanehisa, M., Goto, S., Sato, Y., Kawashima, M., Furumichi, M., and Tanabe, M. (2014) Data, information,

knowledge and principle: back to metabolism in KEGG. *Nucleic Acids Research*. **42**, D199–205
51. Liang, X., Peng, L., Baek, C.H., and Katzen, F. (2013) Single step BP/LR combined Gateway reactions. *BioTechniques*. **55**, 265–268
52. Engler, C., Kandzia, R., and Marillonnet, S. (2008) A one pot, one step, precision cloning method with high throughput capability. *PLoS ONE*. **3**, e3647
53. Williams, I., and Frank, L. (1975) Improved chemical synthesis and enzymatic assay of d1-pyrroline-5-carboxylic acid. *Analytical Biochemistry*. **64**, 85–97
54. Mezl, V. A., and Knox, W. E. (1976) Properties and analysis of a stable derivative of pyrroline-5-carboxylic acid for use in metabolic studies. *Analytical Biochemistry*. **74**, 430–440

Footnotes:

Current address:

B. C. S. and S. L. W.-S. current address is the Department of Biochemistry, Medical College of Wisconsin, 8701 Watertown Plank Rd., Milwaukee, Wisconsin 53226.

The abbreviations used are: NO, nitric oxide; iNOS, inducible nitric oxide synthase; eNOS, endothelial nitric oxide synthase; nNOS, neuronal nitric oxide synthase; sGC, soluble guanylate cyclase; 6PGD, 6-phosphogluconate dehydrogenase; ALDH4A1, Δ^1-pyrroline-5-carboxylate dehydrogenase; COMT, catechol-*O*-methyltransferase; PHGDH, D-3-phosphoglycerate dehydrogenase; ALDOA, Aldolase A; TPI1, triose phosphate isomerase 1; GSNO, *S*-nitrosoglutathione.

Table 1: Initial enzyme target list. Initial list of enzyme targets of *S*-nitrosation, obtained through the combined proteomics and metabolomics approach. Each enzyme on the list is *S*-nitrosated based on the Ishiropoulos proteomics study; the listed substrate is found in overall increased levels and product at decreased levels (or vice versa) of at least 1.4-fold in eNOS knockout mice compared to wild-type mice from the metabolomics. Metabolite *p*-values were not used to generate in this initial list and the most relevant enzyme targets are found in Table S1.

	Enzyme Name	Uniprot Accession Number	Enzyme Commission Number	Primary Substrate	Primary Product
1	2-amino-3-carboxymuconate-6-semialdehyde	Q8R519	4.1.1.45	2-Amino-3-carboxymuconate semialdehyde	2-Aminomuconate semialdehyde
2	2-oxoglutarate dehydrogenase	Q60597	1.2.4.2	Thiamin Diphosphate (ThPP)	2-Carboxy-1-hydroxyproyl-ThPP
3	2-oxoisovalerate dehydrogenase	P50136	1.2.4.4	Thiamine Diphosphate (ThPP)	2-Methyl-1-hydroxybutyl-ThPP, 1 more
4	3 beta-hydroxysteroid dehydrogenase type 5	Q61694	1.1.1.145/5.3.3.1	3β,17β-Dihydroxy-androst-5-ene	Testosterone
5	3-ketoacyl-CoA thiolase	Q8BWT1	2.3.1.16	3-Oxohexanoyl-CoA, or 3-Oxodecanoyl-CoA	Acetyl CoA, 1 more
6	**6-phosphogluconate dehydrogenase**	**Q9DCD0**	**1.1.1.44**	**D-Gluconate-6-phosphate**	**D-Ribulose-5-phosphate**
7	Acyl-coenzyme A thioesterase 1	O55137	3.1.2.2	C16:0-CoA	Palmitic acid
8	Acyl-coenzyme A thioesterase 10	Q32MW3	3.1.2.-	(7Z,10Z,13Z,16Z)-Docosatetraenoyl-CoA	Adrenic Acid
9	Aldehyde dehydrogenase		1.2.1.3	4-Amino-butanal, 1 more	4-Amino-butanoate, 1 more
10	Aldose reductase	P45376	1.1.1.21	Galactitol, 1 more	D-Galactose, 1 more
11	Amine oxidase B	Q8BW75	1.4.3.4	Phenyl-ethylamine, 1 more	Phenyl-acetaldehyde, 1 more
12	Argininosuccinate lyase	Q91YI0	4.3.2.1	L-Argino succinate	Arginine
13	Aspartate aminotransferase	P05202	2.6.1.1/2.6.1.7	L-Aspartate	Oxaloacetate
14	Aspartoacylase-2	Q91XE4	3.5.1.15	N-Formyl-L-aspartate	Aspartate
15	Bifunctional purine biosynthesis protein PURH	Q9CWJ9	2.1.2.3/3.5.4.10	AICAR	FAICAR
16	Carnitine O-palmitoyltransferase 1	Q924X2	2.3.1.21	Hexadecanoyl-CoA	L-Palmitoyl- carnitine
17	Carnitine O-palmitoyltransferase 2	P52825	2.3.1.21	L-Palmitoyl-carnitine	Hexadecanoyl-CoA

18	**Catechol O-methyltransferase**	**O88587**	**2.1.1.6**	**L-Noradrenaline, 1 more**	**L-Normetanephrine, 1 more**
19	Cytochrome P450	Several Possible	1.14.13.-	Several possible	Several Possible
20	Cytochrome P450 27	Q9DBG1	1.14.13.15	3α,7α,12α-Trihydroxy-5β-cholestane	3α,7α,12α-Trihydroxy-5β-cholestan-26-al
21	Cytosol aminopeptidase	Q9CPY7	3.4.11.5/3.4.11.1	L-Cysteinyl-glycine	L-Cysteine
22	**D-3-phosphoglycerate dehydrogenase**	**Q61753**	**1.1.1.95**	**3-Phospho-D-glycerate**	**3-Phospho-hydroxypyruvate**
23	**Delta-1-pyrroline-5-carboxylate dehydrogenase**	**Q8CHT0**	**1.2.1.88**	**L-1-Pyrroline-3-hydroxy-5-carboxylate**	**L-Erythro-4-hydroxyglutamate**
24	Enoyl-CoA hydratase	Q8BH95	4.2.1.17	Crotonoyl-CoA, 1 more	(S)-3-Hydroxybutanoyl-CoA, 1 more
25	Fatty acid synthase	P19096	2.3.1.85	Malonyl CoA	Tetradecanoic acid, 2 more
26	Gamma-glutamyltranspeptidase1	Q60928	2.3.2.2/3.4.19.13/3.4.19.14	LTC4	LTD4
27	GDH/6PGL endoplasmic bifunctional protein	Q8CFX1	1.1.1.47/3.1.1.31	β-D-Glucose-6-phosphate	D-Gluconate-6-phosphate
28	Glutamate decarboxylase 1	P48318	4.1.1.15	L-Aspartate	β-Alanine
29	Glycerol-3-phosphate dehydrogenase	P13707	1.1.1.8	sn-Glycerol-3-phosphate	Glycerone-phosphate
30	Glycine amidinotransferase	Q9D964	2.1.4.1	4-Amino-butanoate	4-Guanidino-butanoate
31	Hydroxyacyl-coenzyme A dehydrogenase	Q61425	1.1.1.35	(S)-3-Hydroxybutanoyl-CoA	Acetoacetyl-CoA
32	Hydroxymethylglutaryl-CoA lyase	P38060	4.1.3.4	(S)-3-Hydroxy-3-methylglutaryl-CoA	Acetoacetate
33	Indolethylamine N-methyltransferase	P40936	2.1.1.49/2.1.1.96	Tryptamine	N-Methyl tryptamine
34	L-lactate dehydrogenase	P06151	1.1.1.27	3-Mercaptopyruvate	3-Mercaptolactate
35	Lambda-crystallin	Q99KP3	1.1.1.45	L-Gulonate	3-Dehydro-L-gulonate

36	Long-chain-fatty-acid--CoA ligase 1	P41216	6.2.1.3	Hexadecanoate	Hexadecanoyl-CoA
37	Neutral alpha-glucosidase C	Q8BVW0	3.2.1.20	β-D-Fructose, 1 more	Sucrose, 1 more
38	Pyruvate dehydrogenase	P35486	1.2.4.1	Thiamin Diphosphate (ThPP)	2-Hydroxyethyl-ThPP
39	Regucalcin	Q64374	3.1.1.17	L-Gulono-1,4-lactone, 1 more	L-Gulonate, 1 more
40	Succinate dehydrogenase	Q8K2B3	1.3.5.1	Succinate	Fumarate
41	Succinyl-CoA:3-ketoacid-coenzyme A transferase 1	Q9D0K2	2.8.3.5	Acetoacetyl-CoA	Acetoacetate
42	UDP-glucuronosyltransferase 1-1	Q63886	2.4.1.17	Testosterone, 3 more	Testosterone glucuronide, 3 more
43	Urocanate hydratase	Q8VC12	4.2.1.49	Urocanate	4-Imidazolone-5-propanoate
44	Xanthine dehydrogenase/oxidase	Q00519	1.17.1.4/1.17.3.2	Paraxanthine, 1 more	1,7-Dimethyluric acid, 1 more

Table 2. Steady-state kinetics. Steady-state kinetic parameters of wild-type and cysteine variants treated with GSNO or GSH. 6PGD and PHGDH at 20 µM and 150 µM, respectively, were treated with 2 mM GSH or GSNO; 20 µM ALDH4A1, ALDOA and TPI-1 were treated with 1 mM GSH or GSNO and 20 µM COMT was treated with 150 µM GSH or GSNO for 1 h at 37 ˚C. All kinetics were performed with at least two independent experiments, each performed with 8 distinct substrate concentrations ran in duplicate, except those denoted with the (*) symbol that indicates one experiment with 8 substrate concentrations was performed. Standard error was reported for error values.

		k_{cat} (s^{-1})	K_M (µM)	k_{cat}/K_M ($\mu M^{-1}s^{-1}$)
6PGD	WT- GSH	18.7 ± 1.2	28.6 ± 6.1	0.678 ± 0.121
	WT-GSNO	0.154 ± 0.056	27.3 ± 1	0.0057 ± 0.0022
	C289S-GSH	22.1 ± 2.5	156 ± 37	0.147 ± 0.019
	C289S-GSNO	0.40 ± 0.1	128 ± 45	0.0033 ± 0.0004
	C366S-GSH	1.91 ± 0.07	50.9 ± 2.6	0.037 ± 0.001
	C366S-GSNO	1.05 ± 0.01	43.4 ± 4.4	0.024 ± 0.003
ALDH4A1	WT-GSH	11.4 ± 0.3	39 ± 1	0.293 ± 0.006
	WT-GSNO	2.39 ± 0.55	121 ± 38	0.021 ± 0.005
	C95S-GSH	9.4 ± 1.0	36.6 ± 0.3	0.257 ± 0.03
	C95S-GSNO	2.78 ± 0.23	187 ± 67	0.0165 ± 0.0046
	C315S-GSH	1.02 ± 0.33	26.9 ± 3.8	0.0369 ± 0.0072
	C315S-GSNO	1.87 ± 0.24	206 ± 25	0.00907 ± 0.00006
		(min^{-1})	(µM)	($\mu M^{-1}min^{-1}$)
COMT	WT-GSH	7.97 ± 0.45	14.7 ± 1.7	0.547 ± 0.036
	WT-GSNO	2.27 ± 0.42	16 ± 1	0.142 ± 0.038
	C223S-GSH	9.5 ± 2.1	26.8 ± 5.7	0.356 ± 0.058
	C223S-GSNO	5.2 ± 1.4	25 ± 2.7	0.208 ± 0.049
	C241S-GSH	8.3*	14*	0.58*
	C241S-GSNO	1.2*	20*	0.063*
		(s^{-1})	(mM)	($mM^{-1}s^{-1}$)
PHGDH	WT-GSH	0.229 ± 0.011	3.03 ± 0.3	0.070 ± 0.004
	WT-GSNO	0.091 ± 0.01	4.41 ± 0.56	0.021 ± 0.001
	C116S-GSH	0.215 ± 0.005	4.01 ± 0.04	0.0536 ± 0.002
	C116S-GSNO	0.146 ± 0.001	3.24 ± 0.36	0.0455 ± 0.005
	C281S-GSH	0.241 ± 0.045	4.78 ± 0.08	0.0502 ± 0.009
	C281S-GSNO	0.066 ± 0.024	5.77 ± 1.27	0.0110 ± 0.0018
		(s^{-1})	(µM)	($\mu M^{-1}s^{-1}$)
ALDOA	WT-GSH	8.4 ± 0.1	20.4 ± 1.2	0.413 ± 0.021
	WT-GSNO	8.6 ± 0.6	20.9 ± 0.3	0.413 ± 0.024
TPI1	WT-GSH	1880 ± 270	901 ± 7	2.09 ± 0.33
	WT-GSNO	1970 ± 90	1010 ± 10	1.96 ± 0.09

Figure Legends

Figure 1. Flow chart used to narrow target enzyme identification for *in vitro* characterization. eNOS-dependent *S*-nitrosated metabolic enzymes were identified in the Ischiropoulos study (23). Metabolites from this metabolomics study with >1.4-fold difference in relative abundance between wild type and *eNOS* knockout mice were also distinguished. These metabolites were plotted on KEGG maps using the program Pathos (32) along with eNOS-dependent *S*-nitrosated enzymes. Enzymes that were *S*-nitrosated and whose substrate was upregulated and product downregulated (or vice versa) were categorized in Table 1. Enzymes whose substrates and products were further distinguished based on *p*-values ($p < 0.1$, n = 6) and confidence in metabolite identification (mass features closely match profiles in METLIN metabolic database) were categorized as enzyme targets that may be functionally affected by *S*-nitrosation in Table S1.

Figure 2. A. Crystal structure of 6PGD (PDB 4GWK). The approximate location of the active site is outlined and faded. A black box highlights the zoomed in region. The zoomed in region highlights the targeted cysteine C366 in red. Annotated active-site catalytic and substrate/cofactor-binding residues are shown in blue. 6PGD C366 is within potential hydrogen-bonding or Van der Waals interaction distances of 3.3 Å to S129 and 3.6 Å to S140 (in green). **B.** 6PGD catalyzes the oxidative decarboxylation of 6-phosphogluconate to ribulose-5-phosphate in the pentose phosphate pathway. In *eNOS*$^{-/-}$ compared to wild type mice, there is a lower abundance of a mass feature consistent with the substrate 6-phosphogluconate in heart and kidney organs as identified with C18 analysis in positive mode and a greater abundance of a mass feature consistent with the product ribulose-5-phosphate in the liver identified with both C18 using negative mode and HILIC using negative mode (see Table S1 for more details). **C.** TAMRA-switch SDS-PAGE gel indicates GSNO-treated 6PGD is *S*-nitrosated while GSH-treated samples exhibit only background fluorescence. Coomassie staining is shown as a loading control. **D.** The specificity constants of 6PGD wild type and variants upon *S*-nitrosation. Comparison of k_{cat}/K_M values in either the presence of GSNO (as the transnitrosation donor in white) or GSH (as a negative control, in grey) (n = 3 for WT and n = 2 for variants with each run including 8 substrate concentrations ran in duplicate). The steady-state kinetic parameters are summarized in Table 1. The procedure exposed 20 μM 6PGD to 2 mM GSH or GSNO for 1 h at 37˚C, buffer exchanging out GSH or GSNO and determining the protein concentration as outlined in the Experimental Procedures section. Comparisons of percent activity are used for GSNO treatments in relation to GSH-treated control. Wild-type 6PGD retains 0.8% activity when treated with GSNO, while cysteine variant C366S (highlighted in red text) is most responsible for *S*-nitrosation-derived inhibition and retains 67% activity when treated with GSNO. Other cysteine mutants were more significantly inhibited by GSNO-treatment with comparable effects as the wild-type 6PGD, including the cysteine C289S, which was identified as *S*-nitrosated in the Ischiropoulos proteomics study (highlighted in blue text). **E-F.** Increasing GSNO concentration leads to increased *S*-nitrosation of cysteine residues responsible for *S*-nitrosation-dependent inhibition, where wild-type 6PGD was exposed to varying concentrations of GSNO for 1 h at 37˚C. **E.** D-switch LC-MS comparisons of select cysteine residues, highlighting the labeling efficiency of *S*-nitrosation with increasing GSNO concentrations. Increased labeling of the cysteine residues responsible for *S*-nitrosation-dependent inhibition, C366, correlates with increased enzymatic inhibition. **F.** Steady-state kinetic analyses highlighting decreased specificity constant values with increasing GSNO concentrations (n = 3). GSH was used as a negative control.

Figure 3. A. Crystal structure of ALDH4A1 (PDB 3V9G). The approximate location of the active site is outlined and faded. A black box highlights the zoomed in region. The zoomed in region highlights the targeted cysteine C315 in red. Annotated active-site catalytic and substrate/cofactor-binding residues are shown in blue. ALDH4A1 C315 is the residue after active-site residue E314 and oriented in a hydrophobic cleft. **B.** ALDH4A1 catalyzes the conversion of L-1-pyrroline-3-hydroxy-5-carboxylate (or Δ^1-pyrroline-5-carboxylate) to 4-hydroxy-L-glutamate (or L-glutamate) in the L-proline degradation pathway. In *eNOS*$^{-/-}$ compared to wild type mice, there is a greater abundance of a mass feature consistent with the substrate L-1-pyrroline-3-hydroxy-5-carboxylate as well as a lower abundance of a mass feature consistent with the

product 4-hydroxy-L-glutamate in the liver where both were identified with HILIC analysis in negative mode (see Table S1 for more details). **C.** TAMRA-switch SDS-PAGE gel indicates GSNO-treated ALDH4A1 is *S*-nitrosated while GSH-treated samples exhibit only background fluorescence. Coomassie staining is shown as a loading control. **D.** The specificity constants of ALDH4A1 wild type and variants upon *S*-nitrosation. Comparison of k_{cat}/K_M values in either the presence of GSNO (as the transnitrosation donor in white) or GSH (as a negative control, in grey) (n = 3 for WT and n = 2 for variants with each run including 8 substrate concentrations ran in duplicate). The steady-state kinetic parameters are summarized in Table 2. The procedure exposed 20 μM ALDH4A1 to 1 mM GSH or GSNO for 1 h at 37˚C, buffer exchanging out GSH or GSNO and determining the protein concentration as outlined in the Experimental Procedures section. Comparisons of percent activity are used for GSNO treatments in relation to GSH-treated control. Wild-type ALDH4A1retains 7% activity when treated with GSNO, while cysteine variant C315S (highlighted in red text) is most responsible for *S*-nitrosation-derived inhibition and retains 25% activity when treated with GSNO. The other cysteine mutant tested, C95S, was more significantly inhibited by GSNO-treatment with comparable effects as the wild-type ALDH4A1. Both C95 and C315 were identified as *S*-nitrosated in the Ischiropoulos proteomics study. **E-F.** Increasing GSNO concentration leads to increased *S*-nitrosation of cysteine residues responsible for *S*-nitrosation-dependent inhibition, where wild type ALDH4A1 was exposed to varying concentrations of GSNO for 1 h at 37˚C. **E.** D-switch LC-MS comparisons of select cysteine residues, highlighting the labeling efficiency of *S*-nitrosation with increasing GSNO concentrations. Increased labeling of the cysteine residues responsible for *S*-nitrosation-dependent inhibition, C315, correlates with increased enzymatic inhibition. **F.** Steady-state kinetic analyses highlighting decreased specificity constant values with increasing GSNO concentrations (n = 3). GSH was used as a negative control.

Figure 4. A. Crystal structure of COMT (PDB 3A7E). The approximate location of the active site is outlined and faded. A black box highlights the zoomed in region. The zoomed in region highlights targeted cysteine C223 in red. Annotated active-site catalytic and substrate/cofactor-binding residues are shown in blue. COMT C223 is located on the surface and by the entrance to the active site of COMT. **B.** COMT *O*-methylates a catechol hydroxyl and has several substrates. In *eNOS*$^{-/-}$ compared to wild type mice, there is a lower abundance of a mass feature consistent with the substrate 2-hydroxy-estradiol-17β in the lung and kidney as identified with C18 analysis in positive mode and a greater abundance of a mass feature consistent with the product 2-methoxy-estradiol-17β in the brain as identified with C18 using positive mode (not shown due to $p > 0.05$) (see Table S1 for more details). **C.** TAMRA-switch SDS-PAGE gel indicates GSNO-treated COMT is *S*-nitrosated while GSH-treated samples exhibit only background fluorescence. Coomassie staining is shown as a loading control. **D.** The specificity constants of COMT wild type and variants upon *S*-nitrosation. Comparison of k_{cat}/K_M values in either the presence of GSNO (as the transnitrosation donor in white) or GSH (as a negative control, in grey) (n = 3 except for C241S, where n = 1 with each run including 8 substrate concentrations including no substrate). The steady-state kinetic parameters are summarized in Table 2. The procedure exposed 20 μM COMT to 150 μM GSH or GSNO for 1 h at 37˚C, buffer exchanging out GSH or GSNO and determining the protein concentration as outlined in the Experimental Procedures section. Comparisons of percent activity are used for GSNO treatments in relation to GSH-treated control. Wild-type COMT retains 26% activity when treated with 150 μM GSNO, while 1 mM GSNO fully eliminates activity. Cysteine variant C223S (highlighted in red text) is most responsible for *S*-nitrosation-derived inhibition and retains 59% activity when treated with GSNO. The other cysteine mutant tested, C241S, was identified as *S*-nitrosated in the Ischiropoulos proteomics study (highlighted in blue text) and was more significantly inhibited by GSNO-treatment.

Figure 5. A. Crystal structure of PHGDH (PDB 2G76). The approximate location of the active site is outlined and faded. A black box highlights the zoomed in region. The zoomed in region highlights targeted cysteine C116 in red. Annotated active-site catalytic and substrate/cofactor-binding residues are shown in blue. PHGDH C116 is at the putative dimer interface and could potentially form a disulfide bond with C116 of its neighboring monomer in the PHGDH homodimer. **B.** PHGDH converts D-3-phosphoglycerate to 3-

phosphohydroxypyruvate in the L-serine biosynthesis pathway and can also convert α-ketoglutarate to the oncometabolite D-2-hydroxyglutarate (not shown). In *eNOS*$^{-/-}$ compared to wild type mice, there is a lower abundance of a mass feature consistent with the substrate D-3-phosphoglycerate in the liver as identified with C18 analysis in negative mode and a greater abundance of a mass feature consistent with the product 3-phosphohydroxypyruvate in the pancreas as identified with HILIC analysis using negative mode (see Table S1 for more details). **C.** TAMRA-switch SDS-PAGE gel indicates GSNO-treated PHGDH is *S*-nitrosated while GSH-treated samples exhibit only background fluorescence. Coomassie staining is shown as a loading control. **D.** The specificity constants of PHGDH wild type and variants upon *S*-nitrosation. Comparison of k_{cat}/K_M values in either the presence of GSNO (as the transnitrosation donor in white) or GSH (as a negative control, in grey) (n = 3 for WT and n = 2 for variants with each run including 8 substrate concentrations ran in duplicate). The steady-state kinetic parameters are summarized in Table 2. The procedure exposed 150 μM PHGDH to 2 mM GSH or GSNO for 1 h at 37˚C, buffer exchanging out GSH or GSNO and determining the protein concentration as outlined in the Experimental Procedures section. Comparisons of percent activity are used for GSNO treatments in relation to GSH-treated control. Wild-type PHGDH retains 29% activity when treated with GSNO, while cysteine variant C116S (highlighted in red text) is most responsible for *S*-nitrosation-derived inhibition and retains 83% activity when treated with GSNO. Other cysteine mutants were more significantly inhibited by GSNO-treatment with comparable effects as the wild-type PHGDH, including the cysteine C281S, which was identified as *S*-nitrosated in the Ischiropoulos proteomics study (highlighted in blue text).

Figure 6. ALDOA and TPI1 were tested as control enzymes that were *S*-nitrosated in the Ischiropoulos proteomics study but did not fit the metabolomics criteria. **A.** TAMRA-switch SDS-PAGE gel indicates GSNO-treated ALDOA and TPI1 are *S*-nitrosated while GSH-treated samples exhibit only background fluorescence. Coomassie staining is shown as a loading control. **B.** As expected, ALDOA and TPI1 were not inhibited by GSNO treatment. Comparison of k_{cat}/K_M values in either the presence of GSNO (as the transnitrosation donor in white) or GSH (as a negative control, in grey) (n = 2). The steady-state kinetic parameters are summarized in Table 1. The procedure exposed 20 μM enzyme to 1 mM GSH or GSNO for 1 h at 37˚C, buffer exchanging out GSH or GSNO and protein concentration determined as outlined in the Experimental Procedures section. Comparisons of percent activity are used for GSNO treatments in relation to GSH-treated control. Wild-type enzymes retain 100% and 91% activity for ALDOA and TPI1, respectively, when treated with GSNO.

Figure 1

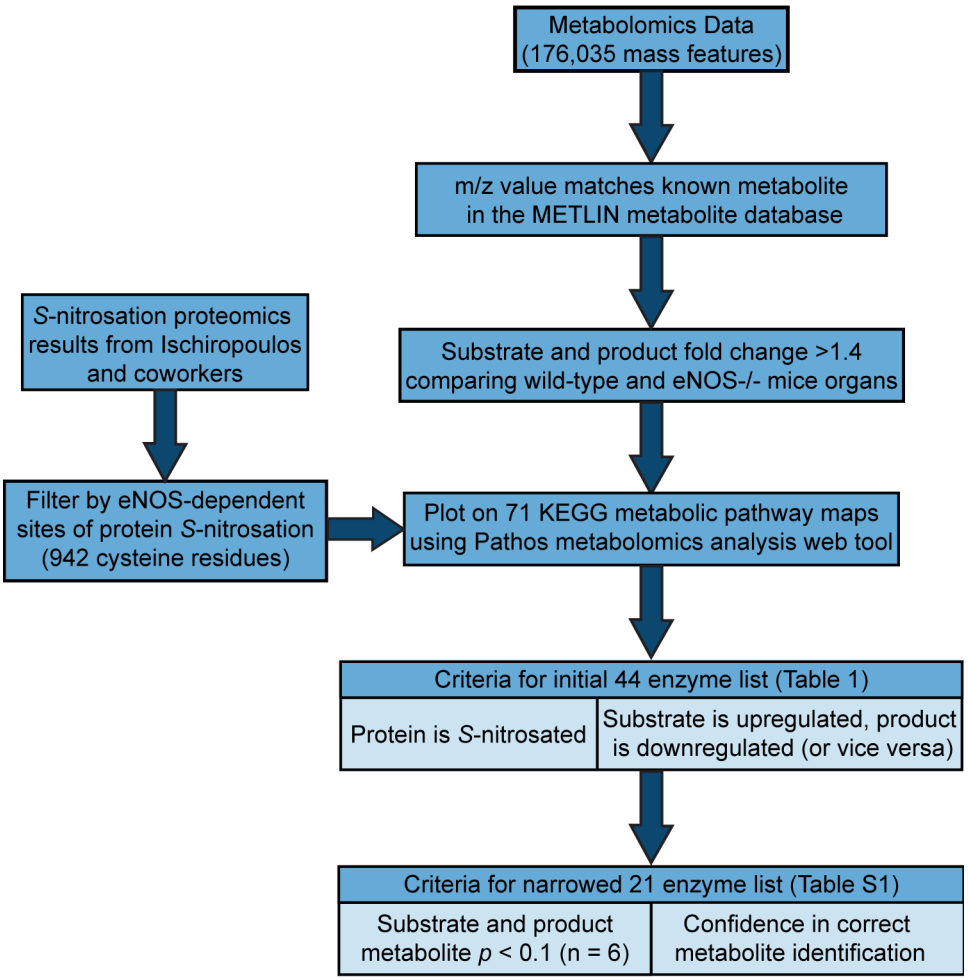

Figure 2

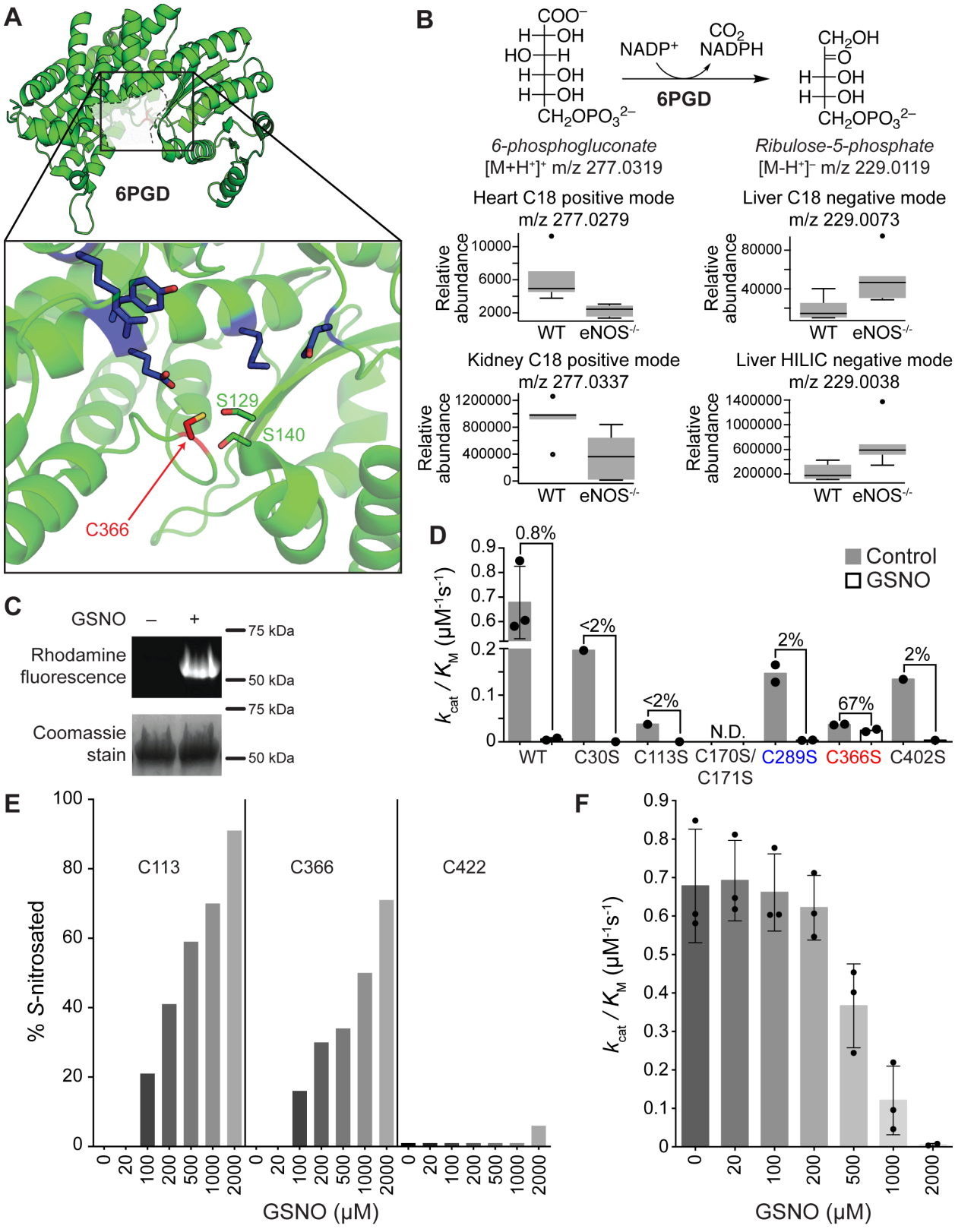

Figure 3

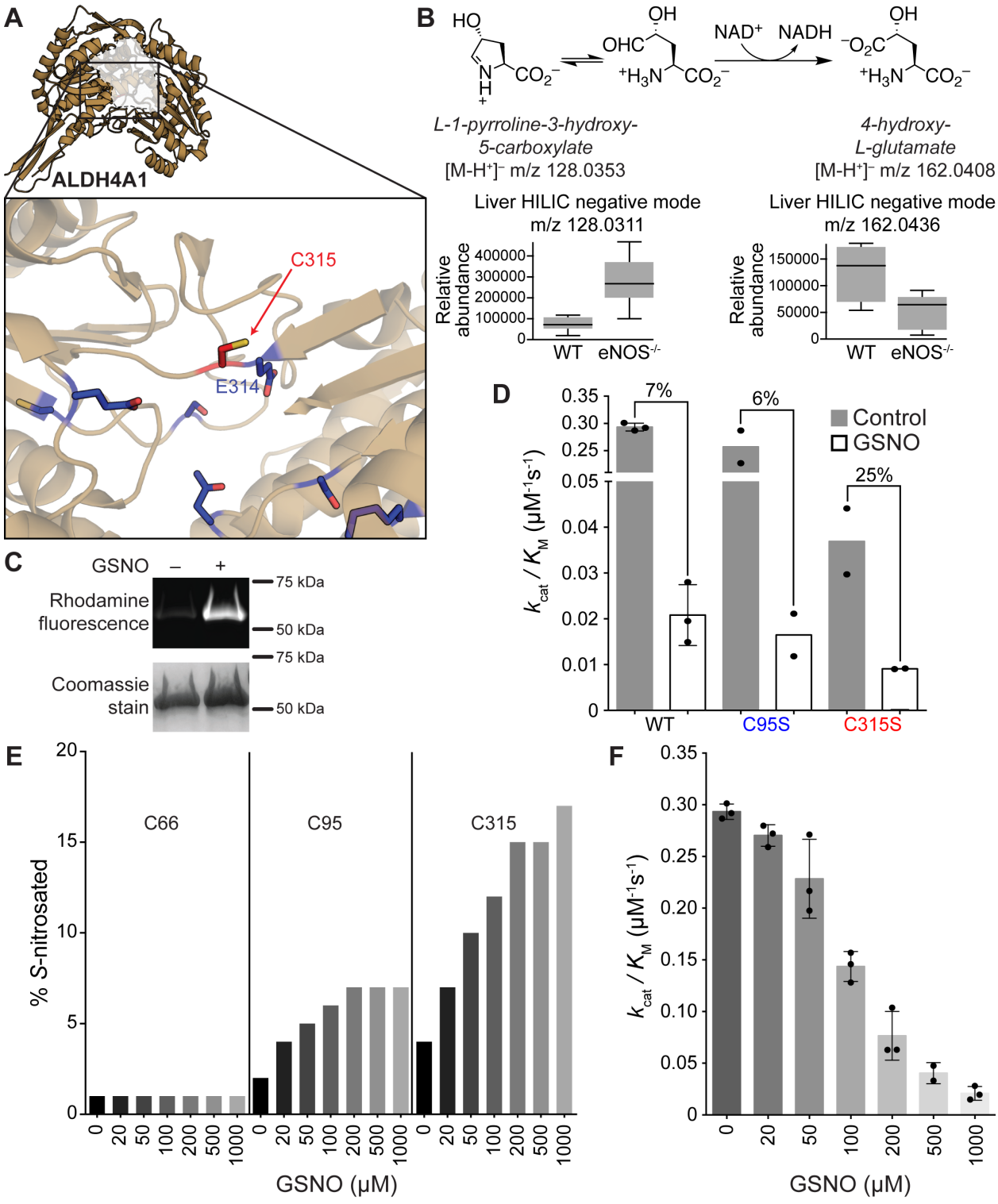

Figure 4

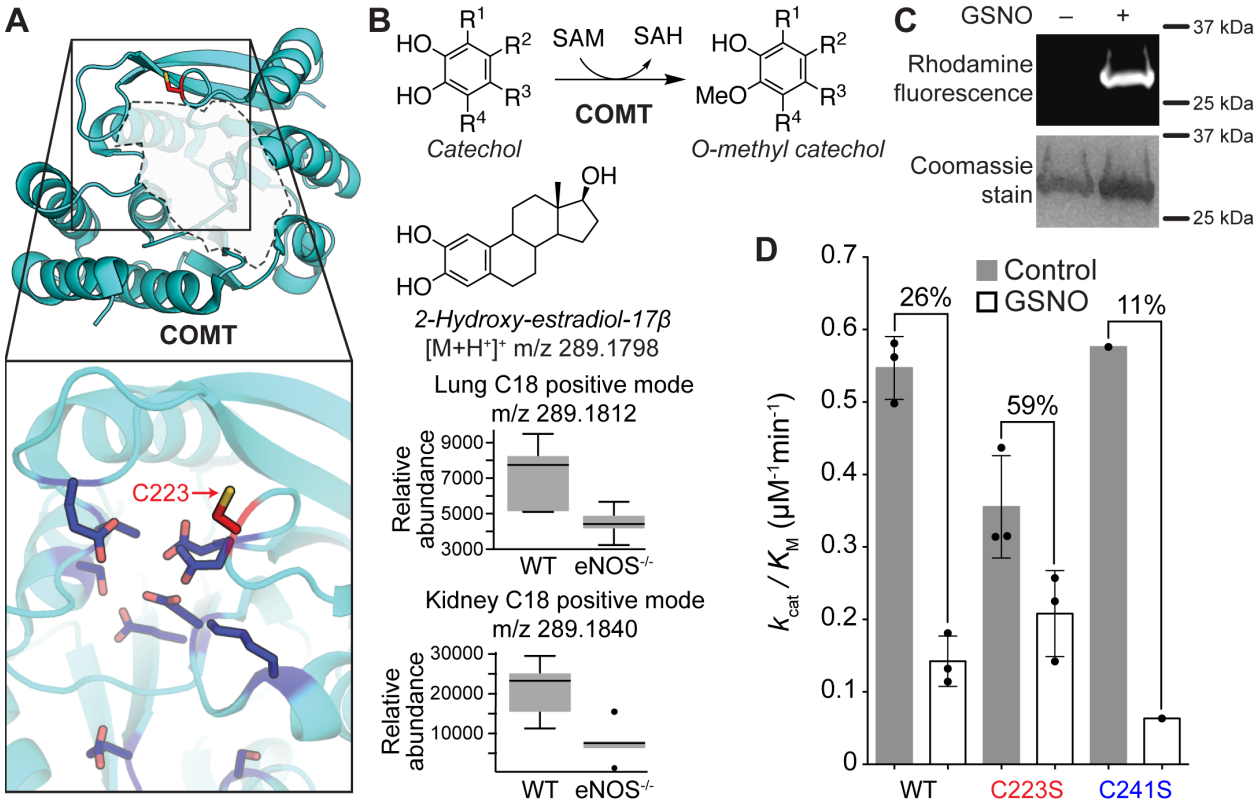

Figure 5

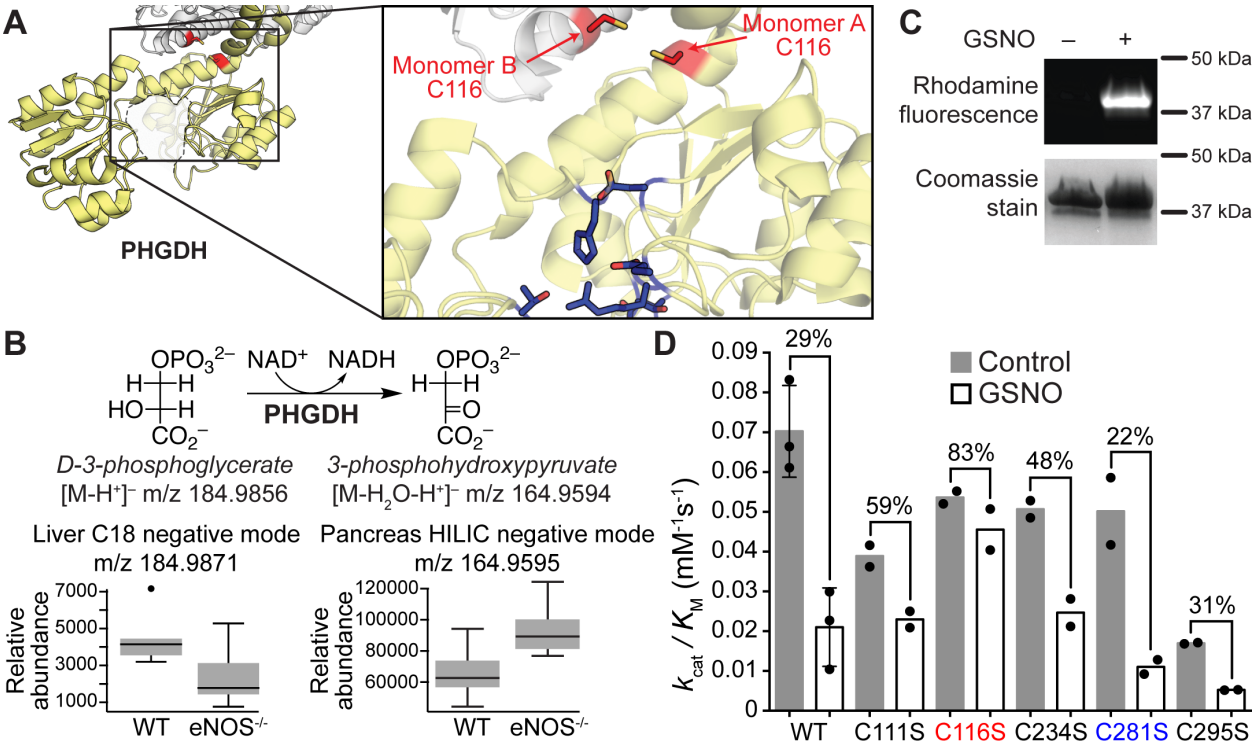

Figure 6

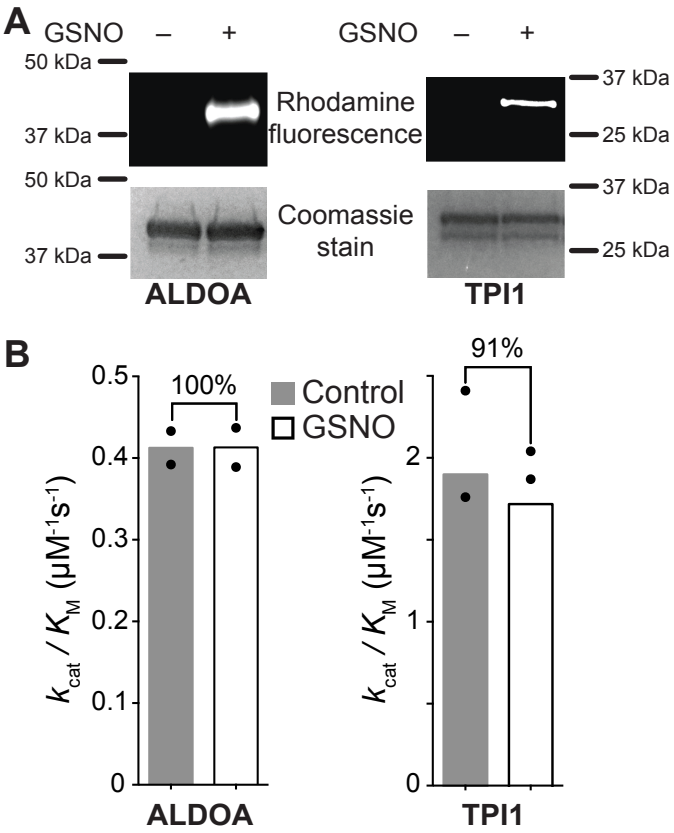

Comparative and integrative metabolomics reveal that S-nitrosation inhibits physiologically relevant metabolic enzymes

Joel J. Bruegger, Brian C. Smith, Sarah L. Wynia-Smith and Michael A. Marletta

J. Biol. Chem. published online February 26, 2018
